

# Interstellar extinction and interstellar polarization: old and new models

N.V. Voshchinnikov

*Sobolev Astronomical Institute, St. Petersburg University, Universitetskii prosp., 28,  
St. Petersburg, 198504 Russia*

---

## Abstract

The review contains an analysis of the observed and model curves of the interstellar extinction and polarization. The observations mainly give information on dust in diffuse and translucent interstellar clouds. The features of various dust grain models including spherical/non-spherical, homogeneous/inhomogeneous particles are discussed. A special attention is devoted to the analysis of the grain size distributions, alignment mechanisms and magnetic field structure in interstellar clouds. It is concluded that the interpretation of interstellar extinction and polarization is not yet complete.

*Keywords:* Light scattering, Nonspherical particles, Composite particles, Extinction, Polarization, Magnetic field

---

## 1. Introduction

The properties of cosmic dust grains in various objects from comets to distant galaxies are derived from observations of interstellar extinction, interstellar polarization, scattered radiation, infrared (IR) continuum emission and IR features. Modelling of these observations is aimed at estimates of the grain size, chemical composition, shape, structure, and alignment. The observed wavelength dependencies of interstellar extinction and polarization (interstellar extinction  $A(\lambda)$  and polarization  $P(\lambda)$  curves) still remain the main sources of information on dust in diffuse and translucent interstellar clouds.

---

*Email address:* [nvv@astro.spbu.ru](mailto:nvv@astro.spbu.ru) (N.V. Voshchinnikov)

In this review, we discuss observations and modelling of the interstellar extinction and polarization curves. Special attention is paid to various dust grain models. For an extended consideration of the properties of dust in different astronomical objects see [1, 2, 3, 4, 5]. Excellent historical reviews on dust astrophysics are given by Dorschner [6] and Li [7].

## 2. Extinction

### 2.1. Extinction curve: production and fitting

The normalized extinction curves  $A^{(n)}(\lambda^{-1})$  commonly studied can be calculated as the ratio of the colour excess of a star behind the dusty cloud  $E(\lambda - V)$  to the colour excess  $E(B - V)$

$$A^{(n)}(\lambda^{-1}) \equiv \frac{E(\lambda - V)}{E(B - V)} = \frac{A(\lambda) - A_V}{A_B - A_V}. \quad (1)$$

Here,  $A_B$  and  $A_V$  is the extinction in the B and V bands, respectively. Sometimes, the normalization of the extinction curve on  $A_V$  or extinction in another band is used.

In such a manner we can determine only the “selective” extinction (reddening), i.e. the difference of extinction at two wavelengths. The absolute value of extinction can be found as

$$A_V = R_V E(B - V), \quad (2)$$

where the coefficient  $R_V$  is often evaluated from observations in the visible and IR taking into account that  $A_\lambda \rightarrow 0$  when  $\lambda \rightarrow \infty$ . From Eq. (1), it follows that

$$R_V = \frac{A_V}{E(B - V)} = -\frac{E(\infty - V)}{E(B - V)}. \quad (3)$$

In the diffuse medium on average  $R_V = 2.4 - 3.6$  [8].

In general, the interstellar extinction curve has a power law-like rise from the IR to the visible, a prominent feature (bump) near  $\lambda 2175 \text{ \AA}$ , and a steep rise in the far-UV. This rise is a manifestation of the very strong feature with a maximum near  $\lambda \approx 700 \text{ \AA}$  [9]. Figure 1 shows the extinction curve averaged over 243 Galactic B and late-O stars [8]. In the near IR-visible part of the spectrum, the distinction between the extinction curves of different stars is rather small. The IR extinction at wavelengths  $\lambda = 0.7\text{--}5 \mu\text{m}$  was approximated by the power-law dependence:  $A(\lambda) \propto \lambda^{-\beta}$  with  $\beta = -1.84$

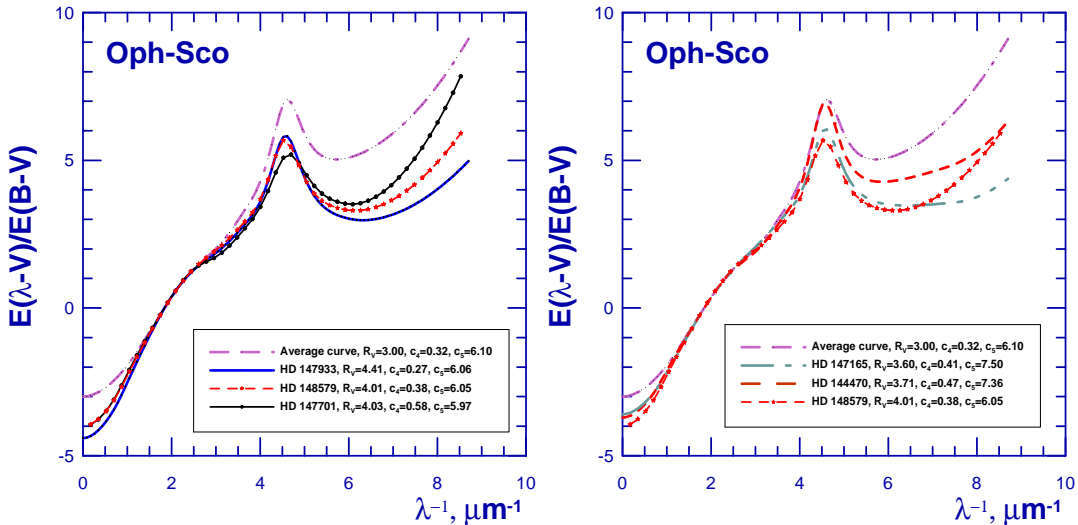


Figure 1: The average extinction curve for 243 Galactic stars with  $2.4 < R_V < 3.6$  and the extinction curves in the direction of six stars in Sco-Oph [8]. The values of the coefficient  $R_V$  and the UV fitting coefficients  $c_4$  and  $c_5$  (Eq. (4)) are indicated in the legend. The effect of variations of coefficients  $c_4$  (left panel) and  $c_5$  (right panel) is illustrated. Adapted from [8].

[10]. Fitzpatrick and Massa [11] found that the index  $\beta$  was  $R_V$ -dependent:  $\beta > 2$  if  $R_V < 3$  and  $\beta < 1.5$  if  $R_V > 3$ . The mid-IR extinction at wavelengths  $\lambda \gtrsim 3 \mu\text{m}$  measured in the Galactic plane [12] and toward the Galactic centre [13] becomes grayer than the near-IR extinction.

In the UV region, the extinction curves differ strongly [8, 14, 15] (see also Fig. 1) demonstrating that the mean curve in the UV obviously has little meaning. The position of the UV bump center varies a little from star to star and occurs at  $\lambda_0 = 2174 \pm 17 \text{ \AA}$  or  $\lambda_0^{-1} = 4.599 \pm 0.012 \mu\text{m}^{-1}$ . The total half-width of the bump is  $W = 0.992 \pm 0.058 \mu\text{m}^{-1}$  that corresponds to  $470 \pm 27 \text{ \AA}$  [16].

Dorschner [17] was the first who suggested to approximate the shape of the bump profile by the classical (Lorentzian) dispersion profile. After examination of the IUE extinction curves for many lines of sight, Fitzpatrick and Massa [8, 16, 18] deduced a single analytical expression with a small number of parameters describing extinction in the region  $1150 \text{ \AA} \leq \lambda <$

2700 Å ( $x \equiv \lambda^{-1}$ )

$$A^{(n)}(x) = \frac{E(\lambda - V)}{E(B - V)} = \begin{cases} c_1 + c_2x + c_3D(x, W, x_0), & x \leq c_5, \\ c_1 + c_2x + c_3D(x, W, x_0) + c_4(x - c_5)^2, & x > c_5, \end{cases} \quad (4)$$

where

$$D(x, W, x_0) = \frac{x^2}{(x^2 - x_0^2)^2 + x^2W^2}. \quad (5)$$

Originally, the value of  $c_5$  was fixed at  $5.9 \mu\text{m}^{-1}$  [18]. Equation (4) consists of: *i*) a Lorentzian-like bump term (requiring three parameters, corresponding to the bump width  $W$ , position  $x_0$ , and strength  $c_3$ ), *ii*) a far-UV curvature term (two parameters  $c_4$  and  $c_5$ ; see Fig. 1 for illustration), and *iii*) a linear term underlying the bump and the far-UV (two parameters  $c_1$  and  $c_2$ ). The parameters of the average extinction curve presented in Fig. 1 are:  $R_V = 3.001$ ,  $x_0 = 4.592 \mu\text{m}^{-1}$ ,  $W = 0.922 \mu\text{m}^{-1}$ ,  $c_1 = -0.175$ ,  $c_2 = 0.807$ ,  $c_3 = 2.991$ ,  $c_4 = 0.319$ ,  $c_5 = 6.097$  [8].

Fitzpatrick and Massa [8] note that there is no correlation between the UV and IR portions of the Galactic extinction curves. This fact is illustrated by Fig. 2 where the dependence of the coefficient  $R_V$  on the quantity describing the strength of the far-UV extinction curvature  $\Delta_{1250} = c_4(8.0 - c_5)^2$  is shown. Absence of the correlation between  $R_V$  and  $\Delta_{1250}$  contradicts the often used representation of the extinction curves from the UV to IR as a one-parameter family dependent on  $R_V$  (so called CCM model introduced by Cardelli, Clayton and Mathis [19, 20]). As mentioned in [8], the relations between  $R_V$  and UV extinction found in [19, 20] can arise from sample selection and methodology. Evidently, some bias relates to the number of clouds available in the line of sight, i.e. to the distance to the star. There exists a wide scatter of the data for nearby stars in comparison with the distant stars (see Fig. 2). A large difference in extinction for the nearby stars observed through single clouds was first noted by Krelowski and Wegner [21]. It should be mentioned that the major part of anomalous or peculiar extinction sight-lines studied so far are related to not very distant stars [22, 23, 24, 25, 26].

## 2.2. Interpretation: homogeneous spheres

The extinction of stellar radiation at the wavelength  $\lambda$  after passing a dust cloud is equal to

$$A(\lambda) = -2.5 \log I(\lambda)/I_0(\lambda) \approx 1.086\tau(\lambda), \quad (6)$$

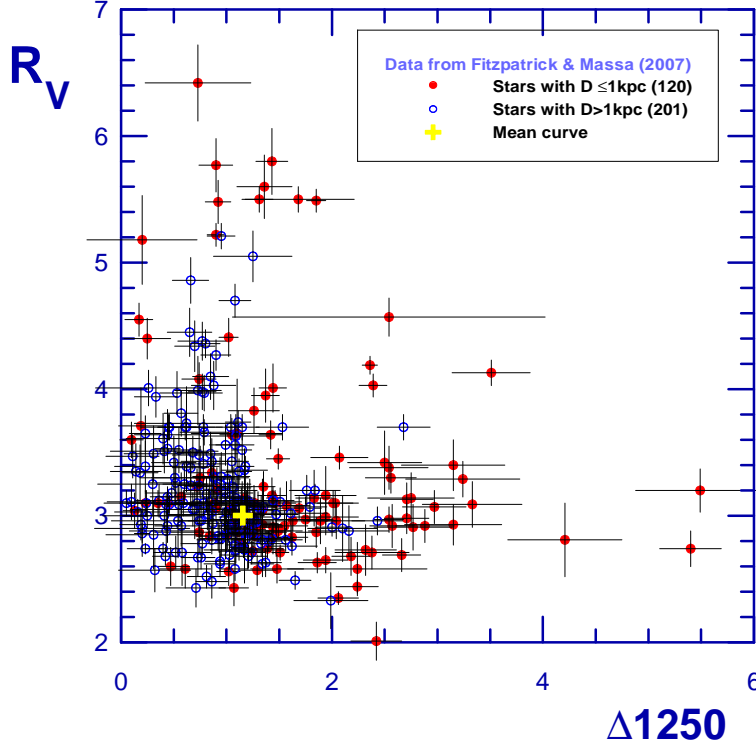


Figure 2: The coefficient  $R_V$  in dependence on the quantity  $\Delta_{1250} = c_4(8.0 - c_5)^2$  showing the strength of the far-UV extinction curvature in the direction of 321 stars with known distances from [8]. Filled and open circles show data for stars with the distances  $D \leq 1$  kpc and  $D > 1$  kpc, respectively. Cross corresponds to the average Galactic extinction curve.

where  $I_0(\lambda)$  is the source (star) intensity,  $\tau(\lambda)$  the optical thickness which can be found as the total extinction cross-section of all particles types along the line of sight in a given direction. Interpretation of the interstellar extinction is often performed using homogeneous spherical particles of various size distributions. Then, the wavelength dependence of extinction can be calculated as

$$A(\lambda) = 1.086 \sum_j \int_0^D \int_{r_{s,\min,j}}^{r_{s,\max,j}} C_{\text{ext},j}(m, r_s, \lambda) n_j(r_s) dr_{s,j} dl. \quad (7)$$

Here,  $n_j(r_s)$  is the size distribution of spherical dust grains of the type  $j$  and radius  $r_s$  with the lower cut-off  $r_{s,\min}$  and the upper cut-off  $r_{s,\max}$ ,  $C_{\text{ext}}(\dots) = \pi r_s^2 Q_{\text{ext}}(\dots)$  the extinction cross-section,  $Q_{\text{ext}}$  the extinction effi-

ciency factor,  $m$  the refractive index,  $D$  the distance to a star. From Eq. (7), an important conclusion follows: the wavelength dependence of interstellar extinction is completely determined by the wavelength dependence of the extinction efficiency  $Q_{\text{ext}}$ .

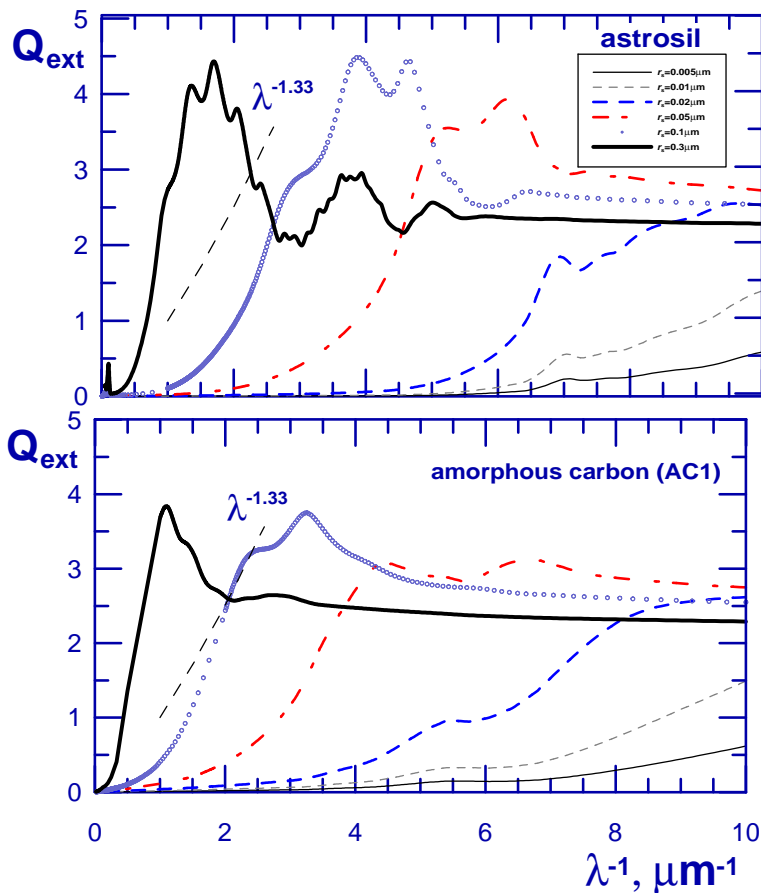


Figure 3: Wavelength dependence of the extinction efficiency factors for homogeneous spherical particles of different sizes consisting of astronomical silicate and amorphous carbon. The dashed segment shows the approximate wavelength dependence of the mean Galactic extinction curve at optical wavelengths. Adapted from [2].

The average interstellar extinction curve in the visible-near UV can be approximated by the power law  $A(\lambda) \propto \lambda^{-1.3}$  [8]. Such wavelength dependence can be produced by submicron-sized particles of the typical radius  $\langle r \rangle \approx 0.05 - 0.1 \mu\text{m}$ . In this case, for more absorbing materials like amorphous carbon or iron we have smaller particles and for less absorbing materials like silicate or ice we need larger particles (see Fig. 3). So, from the

wavelength dependence of extinction only the product of the typical particle size and the refractive index  $\langle r \rangle |m - 1| \approx \text{const.}$  can be determined, but not the size or chemical composition of dust grains separately. In order to solve this problem, the dust-phase abundances of the main elements forming dust (C, O, Mg, Si and Fe) need to be taken into account and to reproduce the absolute extinction. Unfortunately, despite numerous observations of the interstellar absorption lines (see a compilation of Gudennavar et al. [27]) abundances with good accuracy are known just for a restricted number of diffuse and translucent clouds [28, 29, 30].

Another problem having many solutions is identification of the UV bump near  $\lambda 2175 \text{ \AA}$ . Various materials with isotropic and anisotropic properties such as silicate (enstatite), irradiated quartz, oxides (MgO, CaO), organic molecules have been considered as carrier candidates (see discussion in [1, 2]). However, the position and width of the bump are strongly suggestive of  $\pi \rightarrow \pi^*$  transitions in graphitic or aromatic carbonaceous species dominating by  $\text{sp}^2$  bonding. Therefore, small graphite particles and polycyclic aromatic hydrocarbons (PAH molecules) are considered as the favourite materials [31, 32, 33]. Unfortunately, the reliable identification of the carrier remains unknown. The attempts to find the UV or visual bands of PAHs have failed [34, 35]. We cannot even determine the size of graphite spheres responsible for the  $\lambda 2175 \text{ \AA}$  feature (see Fig. 4). The profiles with the central position near  $\lambda_0^{-1} = 4.6 \mu\text{m}^{-1}$  can be obtained if we take particles with the radius  $r_s \approx 0.015 \mu\text{m}$  (Fig. 4, left panel). Although for single-size particles the width of the calculated profiles is smaller than the observed one, a simple bi-modal size distribution allows a fit to both the position and the width of the mean Galactic profile (Fig. 4, right panel).

The far-UV extinction can be explained by tiny particles of the typical radius  $\langle r \rangle \approx 0.01 - 0.03 \mu\text{m}$  (see Fig. 3). The number density of such grains is  $\sim 1000$  times large than the submicron particles producing the visual-near-IR extinction [36]. Because of temperature fluctuations, such particles are protected from growth by accretion in the interstellar clouds. The far-UV rise of extinction may be also fitted as the low-energy side of  $\sigma \rightarrow \sigma^*$  transitions in PAHs (see [37] for discussion).

By using particles of different chemical composition and applying Eq. (7) it is possible to interpret the interstellar extinction and to reconstruct the dust size distribution. In the pioneer work of Oort and van de Hulst [38] the size distribution of icy grains was found in the tabular form. Later, Greenberg [39] fitted it with an exponential function. By using minimiza-

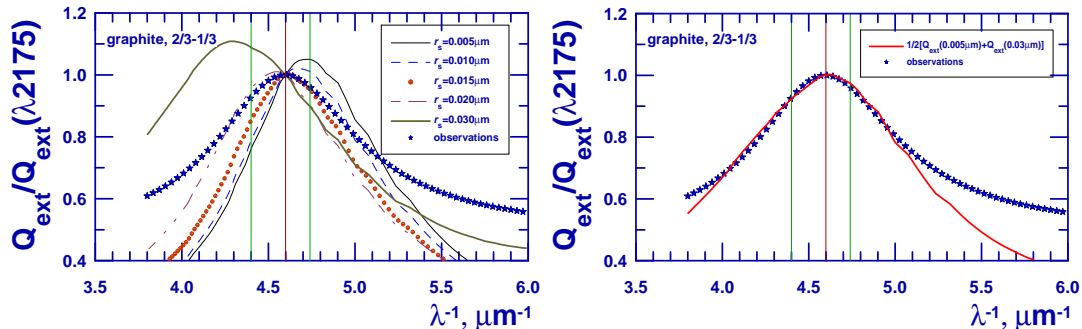


Figure 4: Normalized extinction efficiencies for graphite spheres. The curve marked as “observations” corresponds to the wavelength dependence of the UV bump given by the mean Galactic extinction curve. The central position of the observed UV bump and its range of variations are marked. The left panel shows extinction of single size graphite spheres. The right panel shows the summary extinction of two graphite spheres with radii  $r_s = 0.005 \mu\text{m}$  and  $r_s = 0.03 \mu\text{m}$  (from left panel) taken in equal proportions. All calculations were made in the “2/3–1/3” approximation for the averaged extinction factors  $Q_{\text{ext}} = 2/3 Q_{\text{ext}}(\varepsilon_{\perp}) + 1/3 Q_{\text{ext}}(\varepsilon_{\parallel})$ , where  $\varepsilon_{\perp}$  and  $\varepsilon_{\parallel}$  are the dielectric functions for two cases of orientation of the electric field relative to the basal plane of graphite. Adapted from [2].

tion of the  $\chi^2$  statistic, Mathis et al. [41] reconstructed the power-law size distribution for silicate and graphite particles. These two simplest size distributions contain the only parameter (except for the lower and upper cut-offs, see Table 1). More complicated two-parameter distributions were applied by Wickramasinghe and Guillaume [42] and Wickramasinghe and Nandy [43] in order to fit the mean extinction curve with graphite grains and a mixture of graphite, iron and silicate grains, respectively. A comprehensive discussion of the early attempts to model the interstellar extinction can be found in the review of Wickramasinghe and Nandy [44].

The size distributions of dust grains can be also found from extinction measurements by solving the inverse problem. It has been made by the maximum entropy method [45] and by Tikhonov’s method of regularization [47, 48, 49]. The obtained size distributions were approximated by rather complicated functions containing up to 14 parameters (see Table 1). Complexity of the size distributions used in [31, 47] is explained by the challenge in reproducing the diffuse Galactic IR emission as well.

Table 1: Dust size distributions used for interpretation of interstellar extinction.

Author(s) (year) reference; size distribution function	$N_{\text{parameters}}$
Greenberg (1968) [39]; exponential $n(r_s) \propto \exp[-5 (r_s/r_{s0})^3]$	1
Isobe (1973) [40]; exponential $n(r_s) \propto \exp[-(r_s/r_{s0})]$	1
Mathis et al. (1977) [41]; power-law; MRN mixture $n(r_s) \propto r_s^{-q}$	1
Wickramasinghe and Guillaume (1965) [42]; normal $n(r_s) \propto \exp[-(r_s - \bar{r}_s)^2 / (2\sigma^2)]$	2
Wickramasinghe and Nandy (1971) [43]; lognormal $n(r_s) \propto r_s^{r_1} \exp[-1/2 (r_s/r_2)^3]$	2
Kim et al. (1994) [45]; power-law with exponential decay $n(r_s) \propto r_s^{-\gamma} \exp(-r_s/r_{sb})$	2
Mathis (1996) [46]; power-law with exponential decay $n(r_s) \propto r_s^{-\gamma_0} \exp[-(\gamma_1 r_s + \gamma_2/r_s + \gamma_3/r_s^2)]$	4
Weingartner and Draine (2001) [31]; two lognormal $n(r_s) \propto \mathcal{D}_C(r_s) + \frac{\mathcal{C}_{C, \text{Si}}}{r_s} \left( \frac{r_s}{r_{t; C, \text{Si}}} \right)^{\alpha_{C, \text{Si}}}$ $\times \left\{ \begin{array}{l} 1 + \beta_{C, \text{Si}} r_s / r_{t; C, \text{Si}}, \quad \beta \geq 0 \\ (1 - \beta_{C, \text{Si}} r_s / r_{t; C, \text{Si}})^{-1}, \quad \beta < 0 \end{array} \right\}$ $\times \left\{ \begin{array}{l} 1, \quad 3.5 \text{ \AA} < r_s < r_{t; C, \text{Si}} \\ \exp\{-[(r_s - r_{t; C, \text{Si}})/r_{t; C, \text{Si}}]^3\}, \quad r_s > r_{t; C, \text{Si}} \end{array} \right\}$	11
Zubko et al. (2004) [47]; $\log n(r_s) = c_0 + b_0 \log(r_s) - b_1  \log(r_s/a_1) ^{m_1}$ $- b_2  \log(r_s/a_2) ^{m_2} - b_3  r_s - a_3 ^{m_3} - b_4  r_s - a_4 ^{m_4}$	14

### *2.3. Interpretation: inhomogeneous and composite particles*

Progress in observations, the light scattering and grain growth theories gave rise to new dust models with grains more complicated than homogeneous spheres.

Wickramasinghe [50, 51] was the first who studied the optical properties of core-mantle grains which could grow in interstellar clouds due to accretion of volatile elements on refractory particles. He calculated extinction produced by graphite core-ice mantle and silicate core-ice mantle spheres. Extensive calculations of extinction for graphite core-ice mantle particles were also made by Greenberg [39] who later proposed the existence of particles with silicate cores coated by a layer of organic material in diffuse clouds and silicate-organic-ice grains in molecular clouds [36]. Such grains were a component of the dust mixture reproducing interstellar extinction [52].

The growth of interstellar grains due to their coagulation in dense molecular cloud cores may result in formation of grain aggregates with large voids [53]. The internal structure of such composite grains can be very complicated, and their optical properties cannot be described by the model of core-mantle spheres. Exact calculations are possible for complex aggregates of rather small sizes [54, 55, 56]. Therefore, very complicated particles are replaced by more simple “optically equivalent” ones. A very popular approach is to make calculations using the Mie theory for homogeneous spheres with an average refractive index derived from one of the mixing rules of the effective medium theory (EMT; see, e.g., [46, 47, 57] and Table 2). Another possibility to treat composite aggregate grains is to consider multi-layered particles. As shown by Voshchinnikov and Mathis [60] for spheres and by Farafonov and Voshchinnikov [63] for spheroids, the scattering characteristics of layered particles slightly depend on the order of materials and become close to some “average” ones, when the number of layers exceeds 15 – 20. According to estimates made in [64], the optical properties of layered particles resemble those of heterogeneous particles having inclusions of various sizes while the EMT-Mie approach can be used if the particles have small (in comparison with the wavelength of the incident radiation) “Rayleigh” inclusions.

Inhomogeneous and composite particles have an advantage over homogeneous ones as there exists the possibility of including vacuum as one of the materials. The new dust models with fluffy, porous particles are able to produce the same extinction with a smaller amount of solid material than dust models with compact particles. The amount of vacuum in a particle

Table 2: Models of inhomogeneous spherical grains used for interpretation of interstellar extinction.

Author(s) (year) reference	Model
Wickramasinghe (1963) [50]; Greenberg (1968) [39]	graphite core–ice mantle
Wickramasinghe (1970)[51]	silicate core–ice mantle
Greenberg, Li (1996) [52]	silicate core–organic mantle
Mathis and Whiffen (1989) [57]; Mathis (1996) [46]	EMT-Mie: silicate + amorphous carbon + iron + voids
Zubko et al. (1998, 2004) [47, 49]	EMT-Mie: silicate + organic refractory + water ice + voids
Vaidya et al. (2001) [58]	silicates with graphite inclusions
Voshchinnikov and Mathis (1999) [60]; Voshchinnikov et al. (2006) [61]	multi-layered: vacuum/silicate/ amorphous carbon
Iatì et al. (2008) [62]; Cecchi-Pestellini et al. (2010) [37]; Zonca et al. (2011) [24]	four-layered: vacuum– silicate–sp <sup>2</sup> -carbon– sp <sup>3</sup> -carbon
Rai and Rastogi (2012) [26]	nanodiamonds coated by amorphous carbon or graphite

can be characterized by its porosity  $\mathcal{P}$  ( $0 \leq \mathcal{P} < 1$ )

$$\mathcal{P} = V_{\text{vac}}/V_{\text{total}} = 1 - V_{\text{solid}}/V_{\text{total}}. \quad (8)$$

The role of porosity in extinction is seen from Fig. 5 that gives the wavelength dependence of the normalized cross section

$$C_{\text{ext}}^{(\text{n})} = \frac{C_{\text{ext}}(\text{porous grain})}{C_{\text{ext}}(\text{compact grain of same mass})} = (1 - \mathcal{P})^{-2/3} \frac{Q_{\text{ext}}(\text{porous grain})}{Q_{\text{ext}}(\text{compact grain of same mass})}. \quad (9)$$

This quantity shows how porosity influences the extinction cross section. As follows from Fig. 5, as  $\mathcal{P}$  increases the model predicts a growth of extinction of porous particles in the far-UV and a decrease in the visual–near-UV. In

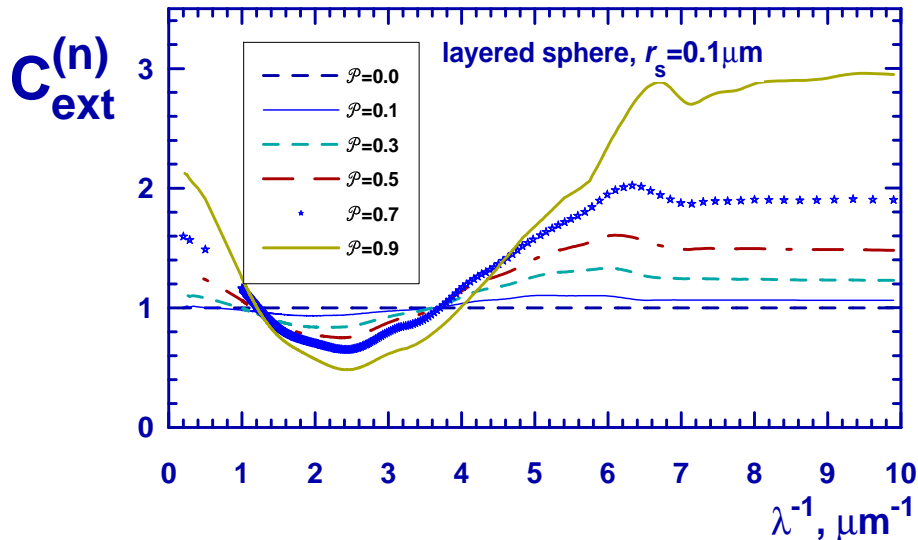


Figure 5: Wavelength dependence of the normalized extinction cross section (see Eq. (9)) for multi-layered spherical particles with  $r_{s, \text{compact}} = 0.1 \mu\text{m}$ . The particles are of the same mass but of different porosity. If  $C_{\text{ext}}^{(n)} > 1$ , extinction of a porous particle is larger than that of a compact one of the same mass. Adapted from [61].

comparison with compact grains, layered particles can also produce rather large extinction in the near-IR. This is especially important for the explanation of the flat extinction across the  $3 - 8 \mu\text{m}$  wavelength range measured for several lines of sight (see [13, 61] for discussion). It is also seen from Fig. 5 that an addition of vacuum into particles does not lead to a growth of extinction at all wavelengths and material saving<sup>1</sup>. Evidently, the final conclusion can be made after detailed comparison of the observations with theoretical calculations at many wavelengths.

Table 2 contains information about models of inhomogeneous spherical grains used for the interpretation of interstellar extinction. Inhomogeneous non-spherical particles of the simplest shapes (cylinders, spheroids) are also used for simultaneous interpretation of interstellar extinction and polarization (see Table 4). In this case major attention has been paid to the modelling

---

<sup>1</sup>This supports a conclusion of Li [65] that an interpretation of the observed interstellar extinction curve using only very porous grains should not give any gain in dust-phase abundances.

of polarization because extinction usually has only a slight dependence on the particle shape and orientation [2, 66].

The models discussed in this Section were first applied to interpreting the average Galactic extinction curve. Modelling of extinction in several sightlines has been also performed [22, 23, 26, 31, 48, 49, 61, 67, 68, 69, 70]. The models include multi-component mixtures of bare particles with a rather complicated size distribution function or/and inhomogeneous particles and PAHs and often took into account abundance restrictions. Especially popular is the direction to the halo star HD 210121 with very high UV extinction. The extinction for this star has been modeled by Li and Greenberg [69] with a mixture of silicate core–organic mantle spheres, bare spheres and PAHs, by Larson et al. [70] and by Clayton et al. [71] with two-component (silicate, graphite) and three-component (silicate, graphite, amorphous carbon) models, by Weingartner and Draine [31] who considered the mixture of carbonaceous and silicate grains with the size distribution given in Table 1, and by Rai and Rastogi [26] who used a silicate-graphite mixture and nanodiamonds coated by carbon. This list illustrates the non-uniqueness of parameters of dust grains obtained from modelling.

A similar conclusion about the ambiguity of the modelling follows from several attempts to interpret the peculiar extinction curves characterized by a broad  $\lambda$  2175 Å bump and a steep far-UV rise or a sharp  $\lambda$  2175 Å bump and flat far-UV extinction (see Fig. 1). Using the model of Weingartner and Draine [31] (see Table 1), Mazzei and Barbaro [23] derived the parameters of the size distribution for 64 stars. Variations of the parameters were attributed to the selective grain destruction in both shocks and grain-grain collisions. Zonca et al. [24] found an excellent fit for different extinction curves for 15 sightlines with the mixture of layered porous grains for reproduction of the near-IR-visual extinction and PAHs to account for the bump and far-UV extinction. Large grains consisting of silicates coated by layers from graphitic and polymeric amorphous carbons (see Table 2) were suggested in the model of Jones et al. [72] (see [73] for more details). Rai and Rastogi [26] analyzed anomalous extinction curves in the direction of 10 stars and showed that a very good match with the far-UV rise of extinction was obtained if to include nanodiamonds coated by graphite or amorphous carbon as a component of the silicate-graphite mixture.

Summarizing this discussion of the interstellar extinction, it should be noted that there is a wide diversity in the models and the non-uniqueness in the results. In spite of numerous attempts to use very complicated inhom-

geneous particles, the Mie theory for homogeneous spheres keeps its leading position as a main tool for the interpretation of interstellar extinction. Further progress in the investigations should include a clear role for PAHs and modelling of the extinction on the basis of interstellar abundances in selected directions. A sophisticated understanding of the origin of UV extinction, the available solid-state material and the grain growth process would stimulate going from simple Mie theory to justified models of complex particles.

### 3. Polarization

#### 3.1. Observations: Serkowski curve and polarizing efficiency

Interstellar linear polarization is caused by the linear dichroism of the interstellar medium due to the presence of non-spherical aligned grains. Dust grains must have sizes close to the wavelength of the incident radiation and specific magnetic properties to efficiently interact with the interstellar magnetic field. The direction of alignment must not coincide with the line of sight and there must be no cancellation of polarization during the propagation of radiation through the interstellar medium.

Interstellar polarization was discovered in 1949 by Hiltner [74], Hall [75] and Dombrovskii [76] in the course of the search for the Sobolev-Chandrasekhar effect<sup>2</sup>. The wavelength dependence of polarization  $P(\lambda)$  in the visible part of spectrum is described by an empirical formula suggested by Serkowski [77]

$$P(\lambda)/P_{\max} = \exp[-K \ln^2(\lambda_{\max}/\lambda)]. \quad (10)$$

This formula has three parameters: the maximum degree of polarization  $P_{\max}$ , the wavelength corresponding to it  $\lambda_{\max}$  and the coefficient  $K$  characterizing the width of the Serkowski curve. Initially, the coefficient  $K$  was chosen by Serkowski [77, 78] to be equal to 1.15<sup>(3)</sup>.

---

<sup>2</sup>Sobolev and Chandrasekhar have shown that the polarization of radiation at the limb of a star due to the electronic (Thomson) scattering should reach  $\sim 12\%$ . Eclipsing binaries with extended atmospheres have been suggested in order to observe the effect.

<sup>3</sup>The Serkowski curve is just one of possible approximations of the observed dependence  $P(\lambda)$ . For example, Wolstencroft and Smith [79] have suggested the representation

$$P(\lambda)/P_{\max} = 2^{\mathcal{K}}(\lambda/\lambda_{\max} + \lambda_{\max}/\lambda)^{-\mathcal{K}}.$$

When  $\mathcal{K} = 2.25$  this curve lies within 1% of the Serkowski curve with  $K = 1.15$  in the wavelength interval  $0.22 - 1.40 \mu\text{m}$ .

The values of  $P_{\max}$  in the diffuse interstellar medium usually do not exceed 10%. The ratios  $P_{\max}/E(B - V)$  and  $P_{\max}/A_V$  determine the polarizing efficiency of the interstellar medium in a selected direction. There exist empirically found upper limits on these ratios [78]

$$P_{\max}/E(B - V) \lesssim 9\%/mag \quad \text{and} \quad P_{\max}/A_V \lesssim 3\%/mag. \quad (11)$$

The mean value of  $\lambda_{\max}$  is  $0.55 \mu\text{m}$  although there are directions for which  $\lambda_{\max}$  is smaller than  $0.4 \mu\text{m}$  or larger than  $0.8 \mu\text{m}$  [80] (see also Fig. 6).

Using observations of about 50 southern stars Whittet and van Breda [81] established a relation between the parameters of the extinction and polarization curves  $R_V = (5.6 \pm 0.3) \lambda_{\max}$ , where  $\lambda_{\max}$  is in  $\mu\text{m}$ . However, further investigations of separate clouds questioned this correlation (e.g., [67, 82, 83]).

The connection between the coefficient  $K$  and the width of the normalized curve of interstellar linear polarization  $W$  is given by the relation

$$W = \exp[(\ln 2/K)^{1/2}] - \exp[-(\ln 2/K)^{1/2}].$$

Treating  $K$  as a third free parameter of the Serkowski curve, Whittet et al. [84] evaluated the dependence between  $K$  and  $\lambda_{\max}$  on the basis of observations for 109 stars

$$K = (1.66 \pm 0.09)\lambda_{\max} + (0.01 \pm 0.05). \quad (12)$$

The coefficients of the linear function (12) for different regions may strongly deviate from the average values (see Fig. 6 where the data for the Taurus dark cloud and the  $\rho$  Oph cloud are plotted).

In parallel with the positive correlation between  $K$  and  $\lambda_{\max}$ , the negative correlation between the polarization efficiency  $P_{\max}/A_V$  and  $\lambda_{\max}$  for stars in separate interstellar clouds and associations is observed [82, 88, 89] (see also discussion in Sect. 3.3).

The IR continuum polarization for  $\lambda > 2.5 \mu\text{m}$  cannot be represented by the Serkowski curve with three parameters. The polarization seems to have a

---

Another approximation has been proposed by Efimov [80]

$$P(\lambda)/P_{\max} = [(\lambda/\lambda_{\max}) \exp(1 - \lambda/\lambda_{\max})]^\beta,$$

where the index  $\beta$  is proportional to  $K$ .

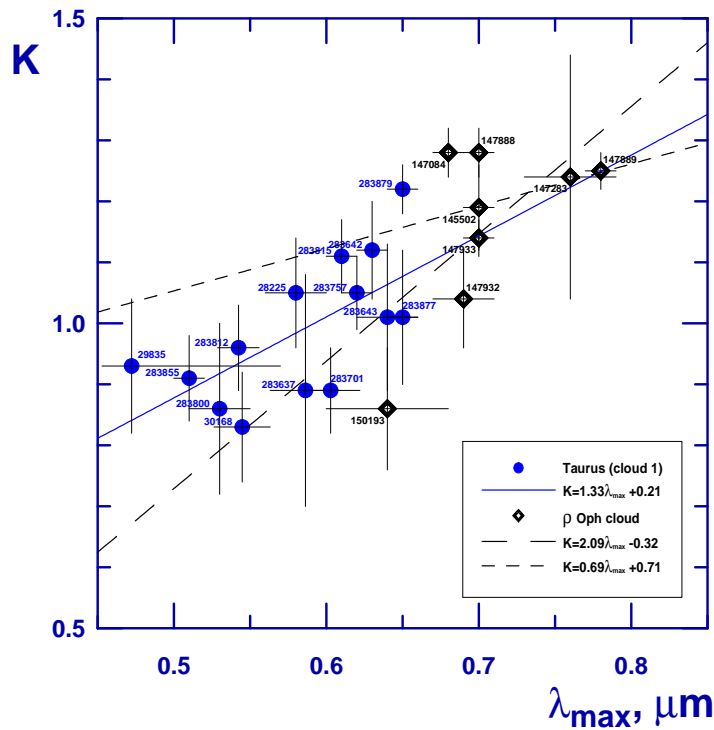


Figure 6: The coefficients  $K$  of the Serkowski curve (10) in dependence on the wavelength of the maximum polarization  $\lambda_{\max}$ . The data were taken from [80, 82] for the Taurus dark cloud and from [85] for  $\rho$  Oph cloud. The HD numbers of stars are marked. Taurus cloud 1 contains 14 stars with similar positional angles of polarization  $\theta_{\text{gal.}} = 145^\circ - 175^\circ$  (see [86] for details). HD 150193 is Herbig Ae/Be star with intrinsic polarization [87]. The linear fits for  $\rho$  Oph cloud are shown for cases with and without HD 150193.

common, universal functional form independent of the value of  $\lambda_{\max}$  and its wavelength dependence is given by a power law  $P(\lambda) \propto \lambda^{-(1.6-2.0)}$  [10, 85]. The UV polarization for 28 lines of sight in the Galaxy has been analyzed by Martin et al. [90] and fitted by a Serkowski-like curve.

As interstellar extinction and interstellar polarization have different wavelength dependencies, the polarizing efficiency  $P(\lambda)/A(\lambda)$  has a maximum in the near-IR. Note that the polarizing efficiency generally increases with wavelength for  $\lambda \lesssim 1 \mu\text{m}$ . It may be approximated by the power-law dependence  $P/A \propto \lambda^\epsilon$ . For stars presented in Fig. 7 the values of  $\epsilon$  vary from 1.41 for HD 197770 to 2.06 for HD 99264.

Variations of the polarizing efficiency in cold dark clouds and star-forming regions are of special interest. It was found that in several dark clouds the

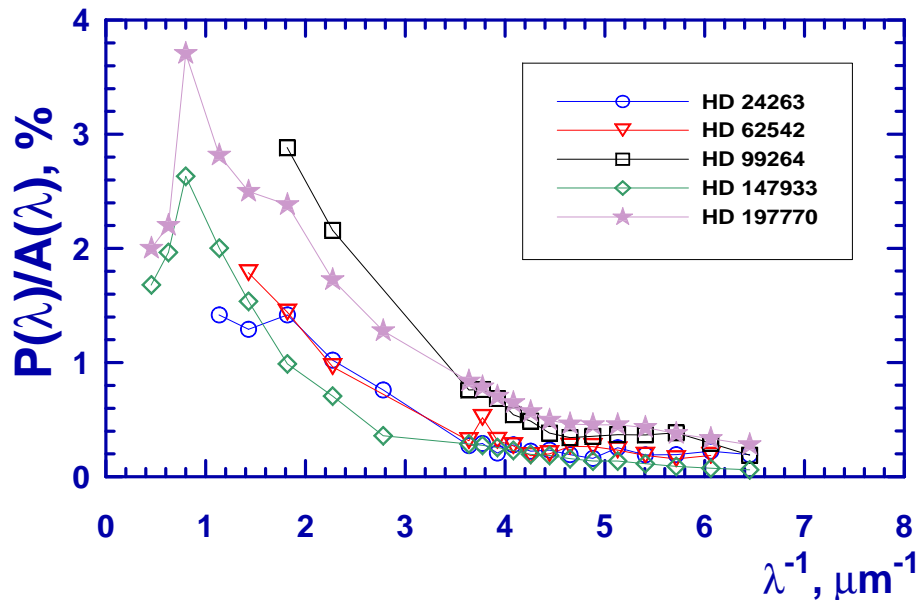


Figure 7: The polarizing efficiency of the interstellar medium in the direction of five stars. Observational data were taken from [14] (extinction) and [91, 92] (polarization). Adapted from [66].

rise of polarization with growing extinction was stopped at some value of  $A_V$  [93, 94] and that the polarizing efficiency  $P_{\max}/A_V$  or  $P_K/A_K$  declines rapidly with increasing extinction [82, 83, 95, 96, 97]. This fact is usually considered as the evidence for the lower efficiency of grain alignment in dark clouds in comparison with diffuse clouds [98]. But it is possible to propound many other factors influencing the polarization degree. They are discussed qualitatively by Goodman et al. [93] (see their Table 4). Nevertheless, there exists the direct evidence for grain alignment in cold dense environments. For example, Hough et al. [99, 100], using spectropolarimetry of the  $3.1 \mu\text{m}$  and  $4.67 \mu\text{m}$  solid  $\text{H}_2\text{O}$  and  $\text{CO}$  features along the line of sight to Elias 16, a field star background to the Taurus dark cloud, found that the features were polarized. This indicates the presence of multi-layered nonspherical grains in molecular clouds because solid  $\text{CO}$  survive at  $T < 20 \text{ K}$  and solid  $\text{H}_2\text{O}$  at higher temperatures.

An error often made is ignoring the foreground polarization. This can be well illustrated by the observational data of Messenger et al. [101] who analysed the interstellar polarization in the Taurus dark cloud. The authors

applied a two-component model and excluded the foreground polarization for star HD 29647. Using the data from Tables 1 and 3 of Messenger et al.

Table 3: Polarization efficiency for stars in Taurus dark cloud\*.

Star	$P_{\max}, \%$	$A_V$	$P_{\max}/A_V, \%$	Comment
HD 283812	6.30	1.91	3.30	cloud 1 (foreground)
HD 29647	2.30	3.32	0.69	clouds 1 + 2
HD 29647	6.17	1.41	4.38	only cloud 2 (background)

\* data from Messenger et al. [101]

[101] it is possible to estimate the polarizing efficiency in the foreground and background clouds. As follows from Table 3, the polarization efficiency in cloud 2 (background) is very high (cf. (Eq. 11)). Therefore, interpretation of the observed polarization instead of the true polarization in the background cloud is a large mistake for HD 29647.

### 3.2. Interpretation: particles and alignment

The interpretation of polarimetric observations includes computations of the polarization cross sections and their averaging over given particles size and orientation distributions. The linear polarization of non-polarized stellar radiation passing through a cloud with a homogeneous magnetic field and rotating particles can be found as (cf. Eq. (7))

$$P(\lambda) = \sum_j \int_0^D \int_{r_{V,\min,j}}^{r_{V,\max,j}} \bar{C}_{\text{pol},j}(m, r_V, \lambda) n_j(r_V) dr_{V,j} dl \cdot 100 \%, \quad (13)$$

$$\bar{C}_{\text{pol},j}(\lambda) = \frac{2}{\pi^2} \int_0^{\pi/2} \int_0^\pi \int_0^{\pi/2} \frac{1}{2} (C_{\text{ext},j}^{\text{TM}} - C_{\text{ext},j}^{\text{TE}}) f_j(\xi, \beta) \cos 2\psi d\varphi d\omega d\beta, \quad (14)$$

where  $n_j(r_V)$  is the size distribution of non-spherical dust grains of the type  $j$ ,  $r_V$  radius of equivolume sphere (for infinite circular cylinders the particle radius  $r_{\text{cyl}}$  is used). The superscripts TM and TE denote two cases of orientation of the electric vector of the incident radiation relative to the particle axis [102]. The average polarization cross sections  $\bar{C}_{\text{pol},j}$  depend on the alignment function  $f(\xi, \beta)$  with the alignment parameter  $\xi$ . Here,  $\beta$  is the



Table 4: Models used for interpretation of interstellar polarization.

Author(s) (year) reference	Dust grains	Alignment (angle)
Wilson (1960) [104]	infinite cylinders*	PDG ( $\Omega = 30^\circ, 90^\circ$ )
Greenberg et al. (1963-8) [39, 105, 106]	infinite cylinders, homogeneous spheroids**	PF, PDG
Rogers and Martin (1979) [107]	homogeneous spheroids	PF ( $\alpha = 90^\circ$ )
Hong and Greenberg (1980) [108]	silicate core–ice mantle infinite cylinders	IDG, PDG
Mathis (1979, 1986) [109, 110]	infinite cylinders*** (spheroids)	PDG <sup>+</sup> ( $\Omega = 90^\circ$ )
Onaka (1980) [111]	core–mantle spheroids	PF ( $\alpha = 90^\circ$ )
Vaidya et al. (1984) [112]	homogeneous spheroids****	PF ( $\alpha = 45^\circ, 90^\circ$ )
Voshchinnikov et al. (1986, 1989) [113, 114]	silicate core–ice mantle infinite cylinders	IDG, PDG
Mishchenko (1991) [115]	homogeneous spheroids	IDG, PDG
Wolff et al. (1993) [116]	homogeneous, coated and composite infinite cylinders, homogeneous spheroids	PDG <sup>+</sup> ( $\Omega = 90^\circ$ )
Kim and Martin (1994) [117]	infinite cylinders	PDG ( $\Omega = 90^\circ$ )
Kim and Martin (1995) [118]	homogeneous spheroids	PF, PDG ( $\alpha, \Omega = 90^\circ$ )
Matsumura and Seki (1996) [119]	homogeneous spheroids and ellipsoids	PF ( $\alpha = 90^\circ$ )
Li and Greenberg (1997) [120]	silicate core–organic mantle finite cylinders	PDG ( $\Omega = 90^\circ$ )
Vaidya et al. (2007) [121]	silicate spheroids with graphite inclusions	PF ( $\alpha = 45^\circ,$ $60^\circ, 90^\circ$ )
Wurm and Schnaiter (2002)	dust aggregates	PF

Table 4: (Continued.)

Author(s) (year) reference	Dust grains	Alignment (angle)
[122]	consisting of 4–64 monomers	( $\alpha = 90^\circ$ )
Voshchinnikov et al. (1990-2010) [66, 123, 124, 103]	homogeneous spheroids	IDG, PDG
Draine and Fraise (2009) [125]	oblate spheroids	PDG <sup>++</sup> ( $\Omega = 90^\circ$ )

PF — picket fence orientation

PDG — perfect Davis–Greenstein (2D) orientation

IDG — imperfect Davis–Greenstein orientation

$\alpha$ , ( $\Omega$ ) — angle between the line of sight and the direction of grain alignment in the case of PF (PDG) orientation

\* in Rayleigh–Gans approximation;

\*\* in Rayleigh approximation;

\*\*\* efficiency factors tabulated by Wickramasinghe [126] were taken; polarization for prolate spheroids was computed as for cylinders;

\*\*\*\* the figures of Asano [127] were used;

+ large silicate grains are assumed to be perfectly aligned (see Eq. (18));

++ only grains with sizes  $r > r_{\text{cut}}$  are assumed to be perfectly aligned (see Eq. (19)).

Early models dealt with homogeneous infinitely long circular cylinders [105, 106, 109, 110]<sup>4</sup>. This is the simplest model of non-spherical particles. Solution to the light scattering problem for infinite cylinders was obtained by the separation of variables method in the cylindrical coordinate system [128]. Later, more advanced models with silicate core-ice mantle cylindrical particles based on the solution from [129] were developed [108, 113, 114]. The progress in the light scattering theory allowed one to apply the model of homogeneous prolate and oblate spheroids of different size and shape for calculations of the polarizing efficiency, visual and UV polarization (see, e.g., [107, 118, 103, 125]). Spheroidal particles are characterized by the aspect ratio  $a/b$  where  $a$  and  $b$  are the major and minor semi-axes. The optical

<sup>4</sup>Another simplification was the use of the wavelength-independent refractive index.

properties of spheroids can be found by using different technique. The most popular methods widely applied in astronomical modelling are the separation of variables method [124, 130], the T-matrix method [115] and the discrete dipole approximation [131]. Comparison of the methods and benchmark results are given in [132, 133]<sup>5</sup>. More complicated non-spherical particles (coated spheroids, ellipsoidal particles, composite spheroids) were considered so far for illustrative calculations [111, 119, 121].

The polarization cross sections must be averaged over rotations taking into account an alignment mechanism. According to standard concepts [1, 134], the alignment of interstellar grains may be magnetic or radiative. A very popular alignment mechanism is the magnetic alignment (Davis–Greenstein (DG) type orientation [135]) based on the paramagnetic relaxation of grain material containing about one percent of iron impurities. For the imperfect Davis–Greenstein (IDG) orientation, the alignment function  $f(\xi, \beta)$  can be written as [108, 114]

$$f(\xi, \beta) = \frac{\xi \sin \beta}{(\xi^2 \cos^2 \beta + \sin^2 \beta)^{3/2}}. \quad (15)$$

The parameter  $\xi$  depends on the particle size  $r_V$ , the imaginary part of the grain magnetic susceptibility  $\chi''$  ( $= \varkappa \omega_d / T_d$ , where  $\omega_d$  is the angular velocity of grain), gas density  $n_g$ , the strength of magnetic field  $B$  and dust ( $T_d$ ) and gas ( $T_g$ ) temperatures

$$\xi^2 = \frac{r_V + \delta_0(T_d/T_g)}{r_V + \delta_0}, \quad \text{where} \quad \delta_0^{\text{IDG}} = 8.23 \cdot 10^{23} \frac{\varkappa B^2}{n_g T_g^{1/2} T_d} \mu\text{m}. \quad (16)$$

If the grains are not aligned  $\xi = 1$  and  $f(\xi, \beta) = \sin \beta$ ; in the case of the perfect rotational orientation  $\xi = 0$ . Unfortunately, only a limited number of models including the combined particle size/shape/orientation analysis have been developed (see Table 4).

For simplicity, many investigators assumed that the direction of the magnetic field (direction of grain alignment) was perpendicular to the line of sight, i.e.,  $\alpha, \Omega = 90^\circ$  (e.g., [110, 118, 125]). Frequently, non-rotating particles of the same orientation are considered (see Table 4). In this case, called the “picket fence” (PF) orientation, there are no integrals over the angles

---

<sup>5</sup>see also Database of Optical Properties (DOP): <http://www.astro.spbu.ru/DOP>

$\varphi$ ,  $\omega$  and  $\beta$  in Eq. (14). The polarization degree is proportional to the polarization cross-section  $P \propto C_{\text{pol}} = 1/2[C_{\text{ext}}^{\text{TM}}(\Omega) - C_{\text{ext}}^{\text{TE}}(\Omega)]$ , where  $\Omega = \alpha$  and  $f(\xi, \beta) = \delta(\alpha)$ <sup>6</sup>. The dichroic polarization efficiency is defined by the ratio of the polarization cross-section (factor) to the extinction one

$$\left(\frac{P}{\tau}\right)_{\text{PF}} = \frac{C_{\text{pol}}}{C_{\text{ext}}} = \frac{C_{\text{ext}}^{\text{TM}} - C_{\text{ext}}^{\text{TE}}}{C_{\text{ext}}^{\text{TM}} + C_{\text{ext}}^{\text{TE}}} \cdot 100\% = \frac{Q_{\text{ext}}^{\text{TM}} - Q_{\text{ext}}^{\text{TE}}}{Q_{\text{ext}}^{\text{TM}} + Q_{\text{ext}}^{\text{TE}}} \cdot 100\%. \quad (17)$$

A more complicated case is the perfect rotational (2D) orientation (or perfect Davis–Greenstein orientation, PDG) when the major axis of a non-spherical particle always lies in the same plane. For the 2D orientation, integration is performed over the spin angle  $\varphi$  only and  $f(\xi, \beta) = \delta(\beta)$ .

Polarization produced by perfectly aligned particles is much larger than that observed (cf. Figs. 9 and 10 with Eq. (11)). Nevertheless, the models with the PF or PDG orientation are useful for investigations of the normalized polarization (the Serkowski curves) as the wavelength dependence of polarization is only slightly influenced by the particle refractive index, size or shape (cf. left panels in Figs. 9 and 10). As a crude approximation of the

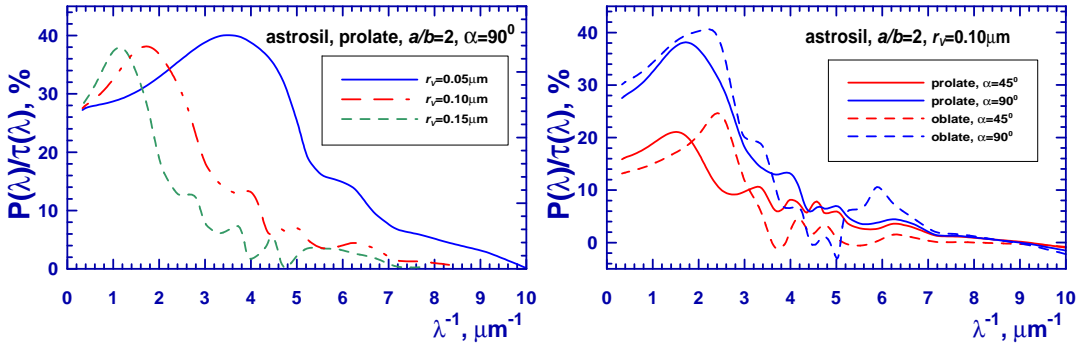


Figure 9: Wavelength dependence of the polarization efficiency for homogeneous spheroids consisting of astrosil for the PF orientation (see Eq. (17)). The effect of variations of the particle size (left panel), type and orientation (right panel) is illustrated. Adapted from [2].

polarization efficiency for particles with the IDG orientation, the following relation is used (see, e.g., [107])

$$\left(\frac{P}{\tau}\right)_{\text{IDG}} = \mathcal{R} \sin^2 \Omega \left(\frac{P}{\tau}\right)_{\text{PF}},$$

<sup>6</sup> $\delta(z)$  is the Dirac delta function.

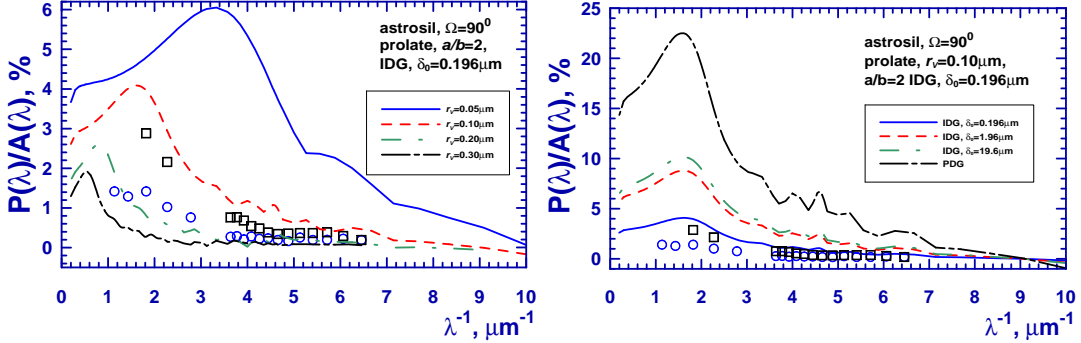


Figure 10: Wavelength dependence of the polarization efficiency for homogeneous rotating spheroidal particles of the astronomical silicate. The effect of variations of particle size (left panel), and degree of alignment (right panel) is illustrated. The open circles and squares show the observational data for stars HD 24263 and HD 99264, respectively. Adapted from [66].

where  $\mathcal{R} = 1/2(3\langle \cos^2 \beta \rangle - 1)$  is the Rayleigh reduction factor [39, 136] and  $\langle \rangle$  denotes the ensemble average. It should be emphasized that application of this approximation as well as the Rayleigh reduction factor can lead to misinterpretation of observational curves  $P(\lambda)$ .

In the case of the IDG mechanism, smaller grains are aligned better than larger grains (see Eq. (16)). However, the models with an opposite type of orientation of small and large particles have been also suggested. Mathis [110] assumed that rotating silicate grains were perfectly aligned if they contain at least one super-paramagnetic inclusion. Carbonaceous grains and silicate grains without inclusions are randomly oriented in space (3D orientation). The probability of perfect alignment is

$$f(r_V, r'_V) = 1 - \exp(-r_V/r'_V)^3. \quad (18)$$

Draine and Fraisse [125] considered the model of silicate and amorphous carbon spheroids with randomly oriented small particles and perfectly aligned large particles. In this case the alignment function is size dependent

$$f(\beta, r_V) = \begin{cases} \sin \beta & \text{for } r_V \leq r_{V,\text{cut}}, \\ \delta(\beta) & \text{for } r_V > r_{V,\text{cut}}, \end{cases} \quad (19)$$

where  $r_{V,\text{cut}}$  is a cut-off parameter.

Computations made by Das et al. [103] (see their Fig. 2) demonstrate that the observational data can be fitted by using the models with different

alignment functions (e.g., given by Eqs. (15), (18) or (19)), especially if a more complex size distribution function as discussed in Sect. 2.2 is chosen. However, this complicates the model. To avoid the models with many parameters new ideas about the nature of polarizing grains and physics of grain alignment should be included.

The DG mechanism of the paramagnetic relaxation requires a stronger magnetic field than average Galactic magnetic field ( $\sim 3 - 5 \mu\text{G}$ ; [137]). Because of this problem, it has been suggested that the polarizing grains contain small clusters of iron, iron sulfides, or iron oxides with super-paramagnetic or ferromagnetic properties [138]. This leads to an enhancement of the imaginary part of the magnetic susceptibility of grain material  $\chi''$  by a factor 10 – 100 and alignment can occur through the DG mechanism. This scenario is supported by laboratory experiments [139, 140]. A significant enhancement of  $\chi''$  is also possible in mixed MgO/FeO/SiO grains [141] or in H<sub>2</sub>O ice mantle grains containing magnetite (Fe<sub>3</sub>O<sub>4</sub>) precipitates [142, 143].

Another possibility to align interstellar grains is the radiative torque alignment (RAT alignment). It arises from an azimuthal asymmetry of the light scattering by non-spherical particles. Magnetic inclusions can enhance RAT alignment [144]. The theory of RAT alignment is well developed [145]. Recent observations of interstellar polarization in the vicinity of luminous stars [146, 147, 148] have been used for confirmation of the RAT alignment mechanism. However, the discussed models are phenomenological, they are not based on correct light scattering calculations of interstellar polarization. One of the reasons is that the alignment function for the RAT mechanism is unknown. Another reason is a requirement of advanced light scattering methods because fast rotation can only occur for grains of very specific (helical) shape [145, 149]. This is highly improbable from the point of view of grain growth in the interstellar medium.

Since both magnetic alignment and radiative alignment depend on iron inclusions, we can expect that polarization and/or polarization efficiency should increase with the growth of iron fraction in dust grains. This idea was investigated by Voshchinnikov et al. [150] by using available data on interstellar polarization and element abundances previously compiled in [29]. It was suggested that the interstellar polarization was probably related to the amount of iron in dust grains. Assuming that all silicon and all magnesium are embedded into amorphous silicates of olivine composition (Mg<sub>2x</sub>Fe<sub>2-2x</sub>SiO<sub>4</sub>, where  $x = [\text{Mg}/\text{H}]_{\text{d}} / (2[\text{Si}/\text{H}]_{\text{d}})$  as is a part of iron. The remaining part of Fe

can be found as

$$[\text{Fe}(\text{rest})/\text{H}]_d = [\text{Fe}/\text{H}]_d - (2 [\text{Si}/\text{H}]_d - [\text{Mg}/\text{H}]_d). \quad (20)$$

As indicated in Fig. 11 (left panel), there is a negative correlation between

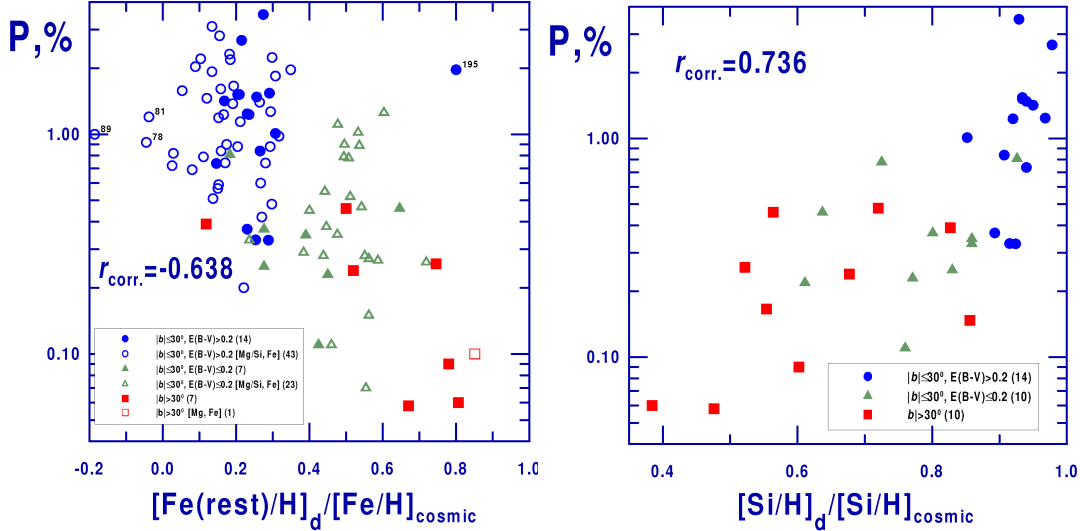


Figure 11: Interstellar polarization in dependence on remaining dust phase abundance of Fe as given by Eq. (20) (left panel) and dust phase abundance of silicon (right panel). Halo stars with  $|b| > 30^\circ$  and disk stars with  $|b| \leq 30^\circ$  and low ( $E(B - V) \leq 0.2$ ) and high ( $E(B - V) > 0.2$ ) reddening are shown with different symbols. Number of stars is indicated in parentheses in the legend. Adapted from [150].

the polarization degree  $P$  and the amount of remaining iron. This is inconsistent with the common suggestion about the great role of iron-rich grains in the production of polarization. Since  $P$  is proportional to the column density of polarizing grains, we can conclude that the increase of the iron content in non-silicate grains does not enhance polarization.

Because in calculating  $[\text{Fe}(\text{rest})/\text{H}]_d$  we removed all Si and Mg and a part of Fe from the dust phase, we expect a positive correlation between the polarization and the abundances of the eliminated elements. There is only a weak correlation between  $P$  and  $[\text{Fe}/\text{H}]_d$  or  $[\text{Mg}/\text{H}]_d$  (see [150] for more discussion) and a strong correlation between  $P$  and  $[\text{Si}/\text{H}]_d$  (Fig. 11, right panel). Therefore, it can be established that polarization is more likely produced by silicates. These findings are evidence in favour of the assumption of Mathis [110] that only the silicate grains are aligned and contribute to the

observed polarization, while the carbonaceous grains are either spherical or randomly aligned. Another verification of this suggestion is the absence of any correlation between the polarization efficiency  $P/E(B-V)$  or  $P/A_V$  and dust phase abundances of elements (see [150]). This is because dust grains of all types (silicate, carbonaceous, iron-rich, etc.) contribute to the observed extinction, while only the silicates seem to be responsible for the observed polarization. Thus, the absence of correlation between  $R_V$  and  $\lambda_{\max}$  (see discussion in Sect. 3.1) can be easily understood. These discoveries can be explained if the silicate grains aligned by the radiative mechanism are mainly responsible for the observed interstellar linear polarization<sup>7</sup>.

Analysing models presented in Table 4, it is possible to say that the major part of models includes perfect grain alignment and one angle of alignment and merely a few of them with the IDG orientation can be used for interpretation of observations of individual stars. Indeed, the previous modelling of interstellar polarization was mainly focused on the explanation of the average wavelength dependence (Serkowski curve) [109, 110, 117, 118]. Only Li and Greenberg [69] applied their model of coated cylinders to explain the normalized polarization curve in the direction of HD 210121 and Das et al. [103] interpreted interstellar extinction and polarization observations of seven stars using a mixture of carbonaceous and silicate spheroids. This fact causes deep dissatisfaction because a great amount of observations of interstellar polarization in different areas exists and continuously grows.

### 3.3. Interpretation: dust grains and magnetic field in the Taurus dark cloud

In this section we present the quantitative interpretation of observations of interstellar polarization for a group of stars<sup>8</sup>. Our model of spheroidal grains with imperfect alignment [66, 103] is supplemented by the subroutine calculating three parameters of the Serkowski curve. We also assume that polarization is mainly produced by silicate grains and the degree of alignment of carbonaceous grains is small (see discussion in previous section).

As an example we refer to the Taurus dark cloud (TDC) — the complex of interstellar clouds where active star formation is in progress. This complex

---

<sup>7</sup>Polarization in IR features also supports the idea of separate populations of polarizing (silicate) and non-polarizing (carbonaceous) grains. This follows from the observed polarization of silicate features at 10  $\mu\text{m}$  and 18  $\mu\text{m}$  and the lack of polarization in the 3.4  $\mu\text{m}$  hydrocarbon feature (see [151, 152] and references therein).

<sup>8</sup>More detailed discussion can be found in [86].

lies sufficiently far from the Galactic plane ( $b \approx -15^\circ$ ) at a distance of  $\sim 140$  pc and comprise several dozens dark nebulae, clouds and clumps [153, 154]. It suffers negligible foreground and background extinction [155, 156] and is the subject of numerous investigations of molecular gas [157, 158, 159, 160, 161].

The polarimetric observations of several hundreds stars in the region around the Taurus dark cloud complex have been performed at visual and red wavelengths [160, 162, 163] and in the H and K bands [95, 164, 165, 166]. The obtained polarization maps give an insight into the structure of the plane-of-the-sky component of interstellar magnetic field but are of little use for studies of grain properties and alignment. To find these latter, the wavelength dependence of polarization must be involved. Whittet et al. [82] presented the polarimetric and photometric observations of 27 stars in a wide spectral range in the TDC ( $l \approx 170^\circ \div 176^\circ$ ,  $b \approx -10^\circ \div -17^\circ$ ) and calculated the fit parameters of the Serkowski curve  $P_{\max}$ ,  $\lambda_{\max}$  and  $K$  as well as the values of  $R_V$ . Our initial analysis of these data is based on the two-component model of Messenger et al. [101] and Whittet et al. [167] (see also discussion of Table 3 in Sect. 3.1). It made possible to form two groups of stars with relatively uniform distribution of positional angles of polarization: cloud 1 (14 stars,  $\theta_{\text{gal.}} = 145^\circ - 175^\circ$ ) and cloud 2 (13 stars,  $\theta_{\text{gal.}} = 2^\circ - 40^\circ$ ).

Firstly, we should concentrate on stars in cloud 1 located inside or behind the “diffuse–screen” component of the TDC. These stars are distributed around Heiles Cloud 2 ( $l \approx 174.4$ ,  $b \approx -13.4$ , area  $15.8 \text{ pc}^2$  [161]) — a dense condensation containing TMC-1 (Taurus molecular cloud). Observational data for stars in the cloud 1 plotted in Figs. 12, 13 indicate positive correlation between  $K$  and  $\lambda_{\max}$  (the width of the polarization curve  $W$  decreases with increasing  $\lambda_{\max}$ ) and negative correlation between the polarization efficiency  $P_{\max}/A_V$  and  $\lambda_{\max}$ . The first dependence is well known (see Fig. 6 and discussion in [84]). Its qualitative explanation is a systematic reduction in the relative number of small, aligned grains in regions of high  $\lambda_{\max}$  [82, 90]. The sole quantitative modelling was attempted by Aannestad and Greenberg [168]. However, to reduce computational efforts they ruled out the integration over the angle  $\omega$  in Eqs. (14) which led to wrong results for  $W$  [114]. A systematic trend toward smaller polarizing efficiency for larger  $\lambda_{\max}$  was detected for nearby stars closely located on the sky [82, 88, 89]. It has been interpreted as a result of the decrease of the angle  $\Omega$  between the direction of the magnetic field and the line of sight [114].

The results of theoretical modelling are shown in Figs. 12, 13 by open cir-

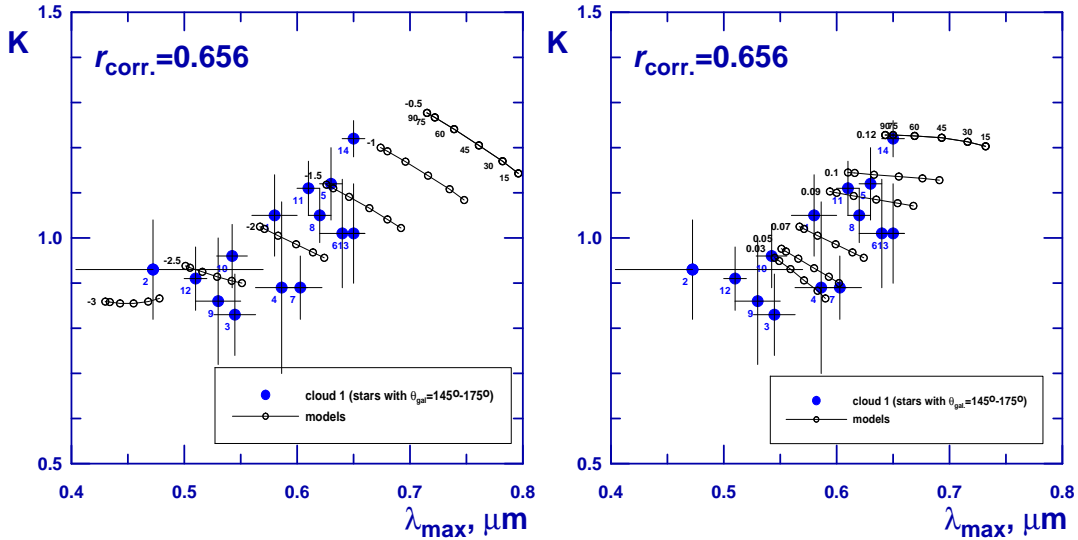


Figure 12: The coefficients  $K$  of the Serkowski curve (10) in dependence on the wavelength of maximum polarization  $\lambda_{\max}$  for 14 stars in cloud 1 in Taurus with the similar positional angles of polarization. The numbers of stars correspond to the increasing HD numbers of stars in Fig. 6, i.e. 1 = HD 28225, ..., 14 = HD 283879. The Pearson correlation coefficient between  $K$  and  $\lambda_{\max}$  is given. Open circles with line show model calculations with different alignment angles  $\Omega = 15^\circ(15^\circ)90^\circ$ . The values of  $\Omega$  increase from right to left as marked for the top model. Left panel illustrates the effect of variations of the power index  $q$  in the power-law size distribution ( $q$  varies from  $-0.5$  to  $-3$ ). Right panel illustrates the effect of variations of the lower cut-off  $r_{V,\min}$  in the power-law size distribution ( $r_{V,\min}$  varies from  $0.03 \mu\text{m}$  to  $0.12 \mu\text{m}$ ). Other model parameters are: prolate spheroids,  $a/b = 3$ ,  $r_{V,\max} = 0.35 \mu\text{m}$ ,  $r_{V,\min} = 0.07 \mu\text{m}$  (left panel),  $q = -2$  (right panel).

cles connected with solid line. The particle shape was fixed: prolate spheroids with the aspect ratio  $a/b = 3$ . Under assumptions made the main parameters of our model influencing the polarization are: the lower and upper cut-offs  $r_{V,\min}$  and  $r_{V,\max}$  and the power index  $q$  in the power-law size distribution for silicate particles and the degree (parameter  $\delta_0^{\text{IDG}}$ , see Eq. (16)) and direction (angle  $\Omega$ ) of alignment. Left and right panels in Fig. 12 illustrate the variations of the index  $q$  and lower cut-off  $r_{V,\min}$ , respectively. The rise of these parameters may be associated with the growth of dust grains by coagulation ( $q$ ) or accretion ( $r_{V,\min}$ ). In both cases the mean size of grains is bigger at the right upper corner of Fig. 12 in comparison with its left bottom corner. It is interesting that the stars NN 1, 5, 6, 8, 11, 14 located at the right upper corner apparently are embedded in Heiles Cloud 2 or situated at its boundary

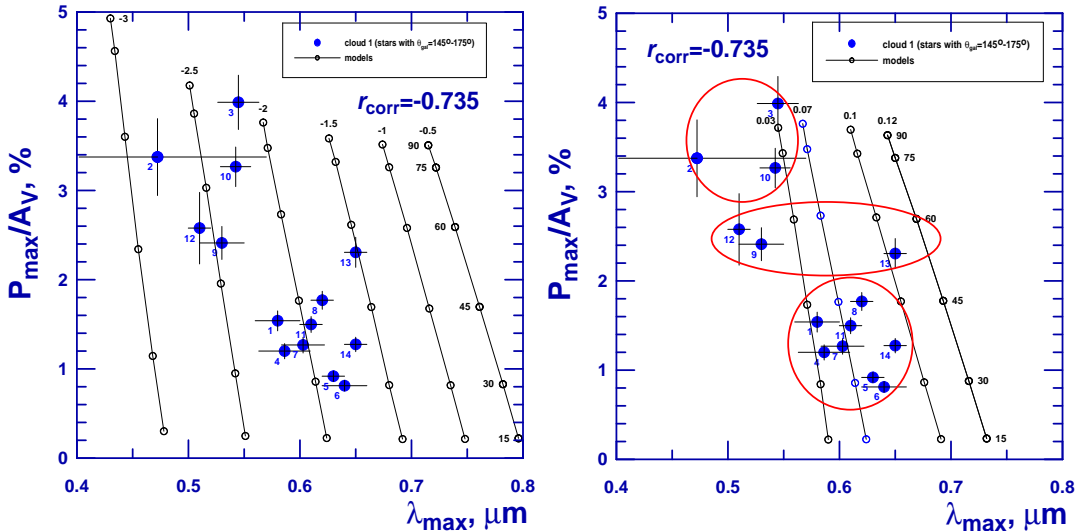


Figure 13: The polarizing efficiency  $P_{\max}/A_V$  in dependence on the wavelength of maximum polarization  $\lambda_{\max}$  for 14 stars in cloud 1 in Taurus. The Pearson correlation coefficient between  $P_{\max}/A_V$  and  $\lambda_{\max}$  is given. Open circles with line show model calculations with different alignment angles  $\Omega = 15^\circ(15^\circ)90^\circ$ . The values of  $\Omega$  increase from bottom to top as marked for the right model. Left panel illustrates the effect of variations of the power index  $q$  in the power-law size distribution ( $q$  varies from  $-0.5$  to  $-3$ ). Right panel illustrates the effect of variations of the lower cut-off  $r_{V,\min}$  in the power-law size distribution ( $r_{V,\min}$  varies from  $0.03 \mu\text{m}$  to  $0.12 \mu\text{m}$ ). Other model parameters are: prolate spheroids,  $a/b = 3$ ,  $r_{V,\max} = 0.35 \mu\text{m}$ ,  $r_{V,\min} = 0.07 \mu\text{m}$  (left panel),  $q = -2$  (right panel).

(see Fig. 14). Note also that variations of alignment parameters  $\delta_0^{\text{IDG}}$  and  $\Omega$  only do not allow explaining the observed correlation between  $K$  and  $\lambda_{\max}$ .

The opposite situation occurs with the correlation between the polarization efficiency  $P_{\max}/A_V$  and  $\lambda_{\max}$  (Fig. 13). In this case to explain both high and low values of  $P_{\max}/A_V$  it is not sufficient to change the grain size only, variations of parameters  $\delta_0^{\text{IDG}}$  and  $\Omega$  must be taken into account. The theoretical points plotted in Fig. 13 were obtained for  $\delta_0^{\text{IDG}} = 3 \mu\text{m}$ . Smaller values of  $\delta_0^{\text{IDG}}$  do not reproduce the data for directions with high polarization efficiency (stars NN 2, 3, 10). It is evident that the obtained grain parameters are model-dependent (e.g., it is possible to use particles of another shape). However, with our model of interstellar dust the trends in variations of the grain size, shape, alignment can be determined.

We attribute the variations of  $P_{\max}/A_V$  in Fig. 13 to the changes in the direction of magnetic field (direction of grain alignment). Stars can be di-

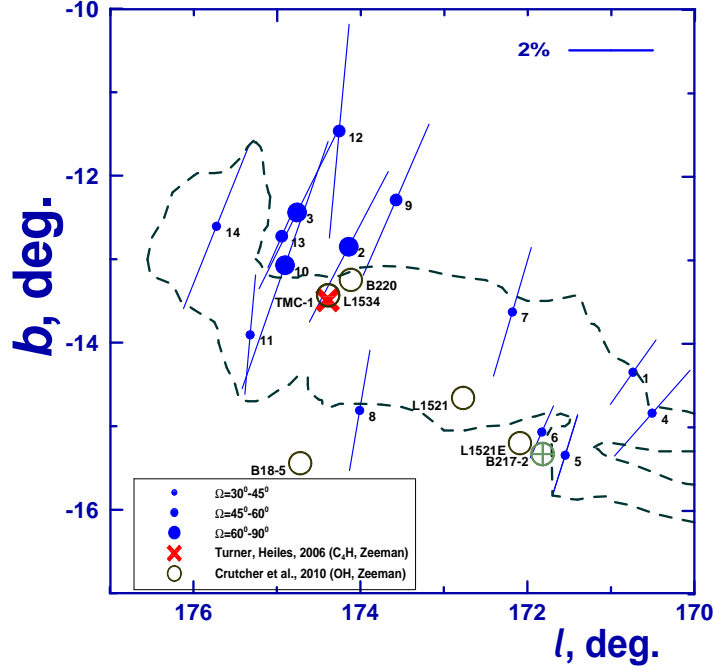


Figure 14: Linear polarization map of the cloud 1 in Taurus containing 14 stars with similar positional angles. The lengths of the lines are proportional to the percent polarization. The sizes of the circles are proportional to the alignment angle  $\Omega$ . The dashed contour represents the regions with different visual extinction:  $1^m6 < A_V < 19^m6$  inside contour and  $0^m4 < A_V < 1^m6$  outside contour [156, 169]. The cross corresponds to the clump in TMC-1 where Turner and Heiles [170] have searched the  $C_4H$  Zeeman effect. The open circles show the positions of dark clouds where the OH Zeeman effect has been observed [171].

vided into three groups with close values of  $\Omega$  (see right panel in Fig. 13). These groups of stars are shown in Fig. 14 by filled circles of different sizes. This Figure gives the positions and polarization of stars in cloud 1 and approximate contours of Heiles Cloud 2. It is intriguing that all six stars with the larger values of  $\Omega$  (the magnetic field is mainly perpendicular to the line of sight) are closely located on the sky outside of Heiles Cloud 2. Other eight stars where the magnetic field is significantly tilted to the line of sight are situated near the boundary of the cloud. An indirect support to our interpretation is provided by Zeeman observations. Turner and Heiles [170] obtained an upper limit for magnetic field toward the cold dense TMC-1 cyanopolyne peak core  $B_{\parallel} = B \cos \Omega = 14.5 \pm 14 \mu G$ . A possible reason for this result is

that the magnetic field is directed close to the plane of the sky. Crutcher et al. [171] compiled the Zeeman data for many dark clouds. Several of them located near or inside Heiles Cloud 2 are marked as large open circles in Fig. 14. In almost all cases the data are within  $1\sigma$  error. Only for B217-2 (close to the positions of stars NN 5, 6) the component of the magnetic field parallel to the line of sight has been detected ( $B_{\parallel} = 13.5 \pm 3.7 \mu\text{G}$ ).

The structure and evolution of magnetic field in Heiles Cloud 2 have been discussed by Heyer et al. [160] and Tamura et al. [164]. It was suggested that the contraction and formation of the cloud from the placental Taurus dark cloud with homogeneous magnetic structure occurred along the magnetic field. The gas motions in Heiles Cloud 2 can be described in terms of a rotating ring with the rotation axis coinciding with the magnetic field [157]. Our findings infer that the magnetic field is tilted with respect to the line of sight at the boundaries of Heiles Cloud 2, i.e., magnetic field has a spindel-like structure. Apparently, the area disturbed by contraction of Heiles Cloud 2 terminates at the place where the magnetic field is almost perpendicular to the line of sight (stars NN 2, 3, 9, 10, 12, 13).

#### 4. Conclusions

All modern investigations of cosmic dust in protoplanetary disks, dense clouds, distant galaxies are based on the modelling of “classical” observations of the interstellar extinction and polarization. Our examination shows that the interpretation of these basic observations still remains incomplete. New generation models should include a consideration of interstellar abundances in given directions and accurate treatment of light scattering by physically feasible particles with realistic alignment.

#### Acknowledgments

I am grateful to organizers F. Borghese, M.A. Iatì and R. Saija for inviting me to present this review. I am thankful to the referees for useful comments, L. Cambrésy and P. Padoan for sending the extinction map in numerical form, I.S. Yakovlev and H.K. Das for assistance in calculations and to V.B. Il'in for production Serkowski fitting subroutine and careful reading of manuscript. The work was partly supported by the grant RFBR 10-02-00593a of the Russian Federation.

## References

- [1] Whittet DCB. *Dust in the Galactic Environments*. 2nd ed. Bristol: Institute of Physics Publishing; 2003.
- [2] Voshchinnikov NV. Optics of Cosmic Dust. I. *Astrophys Space Phys Rev* 2004;12:1–182.
- [3] Witt AN, Clayton GC, Draine BT, editors. *Astrophysics of Dust*. ASP Conf. Ser. 309, 2004.
- [4] Henning Th, Grün E, Steinacker J, editors. *Cosmic Dust – Near and Far*. ASP Conf. Ser. 414, 2009.
- [5] Henning Th, editor. *Astromineralogy*. 2nd ed. Heidelberg: Springer; Lect Notes Phys 815, 2010.
- [6] Dorschner J. From dust astrophysics towards dust mineralogy — a historical review. In: Henning Th, editor. *Astromineralogy*, 2nd ed. Heidelberg: Springer; 2010, Lect Notes Phys 815, p. 1–60.
- [7] Li A. Interstellar Grains — The 75<sup>th</sup> Anniversary. In: Saija R, Cecchi-Pestellini C, editors, *Light, Dust and Chemical Evolution*. Bristol: Institute of Physics Publishing; J. Phys. Conf. Ser. 2005;6:229–248.
- [8] Fitzpatrick EL, Massa DL. An Analysis of the Shapes of Interstellar Extinction Curves. V. The IR-Through-UV Curve Morphology. *Astrophys J* 2007;663:320–341.
- [9] Voshchinnikov NV, Il'in VB. Interstellar extinction curve in the far and extreme ultraviolet. *Sov Astron* 1993;37:21–25.
- [10] Martin PG, Whittet DCB. Interstellar extinction and polarization in the infrared. *Astrophys J* 1990; 357:113–124.
- [11] Fitzpatrick EL, Massa DL. An Analysis of the Shapes of Interstellar Extinction Curves. VI. The near-IR extinction law. *Astrophys J* 2009;699:1209–1222.
- [12] Indebetouw R, Mathis JS, Babler BL, Meade MR, Watson C, Whitney BA. et al. The wavelength dependence of interstellar extinction from 1.25 to 8.0  $\mu\text{m}$  using GLIMPSE data. *Astrophys J* 2005;619:931–938.

- [13] Fritz TK, Gillessen S, Dodds-Eden K, Lutz D, Genzel R, Raab W. et al. The derived infrared extinction toward the Galactic center. *Astrophys J* 2011;737:73(21pp).
- [14] Valencic LA, Clayton GC, Gordon KD. Ultraviolet extinction properties in the Milky Way. *Astrophys J* 2004;616:912–924.
- [15] Gordon KD, Cartledge S, Clayton GC. *FUSE* measurements of far-ultraviolet extinction. III. The dependence on  $R(V)$  and discrete feature limits from 75 Galactic sightlines. *Astrophys J* 2009;705:1320–1335.
- [16] Fitzpatrick EL, Massa DL. An Analysis of the Shapes of Interstellar Extinction Curves. I. The 2175 Å bump. *Astrophys J* 1986;307:286–294.
- [17] Dorschner J. Properties of the  $\lambda$  2200 Å interstellar absorber. *Astrophys Sp Sci* 1973;25:405–411.
- [18] Fitzpatrick EL, Massa DL. An Analysis of the Shapes of Interstellar Extinction Curves. III. An atlas of ultraviolet extinction curves. *Astrophys J Suppl Ser* 1990;72:163–189.
- [19] Cardelli JA, Clayton GC, Mathis JS. The determination of ultraviolet extinction from optical and near-infrared. *Astrophys J* 1988;329:L33–L37.
- [20] Cardelli JA, Clayton GC, Mathis JS. The relationship between infrared, optical, ultraviolet extinction. *Astrophys J* 1989;345:245–256.
- [21] Krełowski J, Wegner W. Interstellar extinction curves originated in single clouds. *Astron Nachr* 1989;310:281–287.
- [22] Mazzei P, Barbaro G. Dust properties along anomalous extinction curves. *Mon Not R Astron Soc* 2008;390:706–714.
- [23] Mazzei P, Barbaro G. Dust properties along anomalous extinction curves. II. Studying extinction curves with dust models. *Astron Astrophys* 2011;527:A34(16pp).
- [24] Zonca A, Cecchi-Pestellini C., Mulas G, Malocci G. Modelling peculiar extinction curves. *Mon Not R Astron Soc* 2011;410:1932–1938.

- [25] Krelowski J, Strobel A. Limited diversity of the interstellar extinction law. *Astron Nachr* 2012;333:60–70.
- [26] Rai RK, Rastogi S. Modeling anomalous/non-CCM extinction using nanodiamonds. *Mon Not R Astron Soc* 2012; doi: 10.1111/j.1365-2966.2012.21109.x.
- [27] Gudennavar SB, Bubbly SG, Preethi K, Murthy J. A compilation of interstellar column densities. *Astrophys J Suppl Ser* 2012;199:8(14pp).
- [28] Jenkins EB. A unified representation of gas-phase element depletions in the interstellar medium. *Astrophys J* 2009;700:1299–1348.
- [29] Voshchinnikov NV, Henning Th. From interstellar abundances to grain composition: the major dust constituents Mg, Si, and Fe. *Astron Astrophys* 2010;517:A45(15pp).
- [30] Parvathi VS, Sofia UJ, Murthy J, Babu SRS. Understanding the role of carbon in ultraviolet extinction along Galactic sight lines. *Astrophys J* 2012;in press.
- [31] Weingartner JC, Draine BT. Dust grain-size distribution and extinction in the Milky Way, Large Magellanic Cloud, and Small Magellanic Cloud. *Astrophys J* 2001;548:296–309.
- [32] Li A, Draine BT. Infrared emission from interstellar dust. II. The diffuse interstellar medium. *Astrophys J* 2001;554:778–802.
- [33] Cecchi-Pestellini C, Malocci G, Mulas G, Joblin C, Williams DA. The role of the charge state of PAHs in ultraviolet extinction. *Astron. Astrophys* 2008;486:L25–L29.
- [34] Clayton GC, Gordon KD, Salama F, Allamandola LJ, Martin PG, Snow TP. et al. The role of polycyclic aromatic hydrocarbons in ultraviolet extinction. I. Probing small molecular polycyclic aromatic hydrocarbons. *Astrophys J* 2003;592:947–952.
- [35] Gredel R, Carpenter Y, Rouillé G, Steglich M, Huisken F, Henning Th. Abundances of the PAHs in the ISM: confronting observations with experimental results. *Astron. Astrophys* 2011;530:A26(15pp).

- [36] Greenberg JM. Interstellar Grains. In: McDonnell JAM, editor. *Cosmic Dust*, New York: Wiley; 1978, p. 187–294.
- [37] Cecchi-Pestellini C, Cacciola A, Iatì MA, Saija R, Borghese F, Denti P. et al. Stratified dust grains in the interstellar medium – II. Time-dependent interstellar extinction. *Mon Not R Astron Soc* 2010;408:535–541.
- [38] Oort JH, van de Hulst HC. Gas and smoke in interstellar space. *Bull Astron Inst Netherlandes* 1946;10:187–204.
- [39] Greenberg JM. Interstellar Grains. In: Middlehurst BM, Aller LH, editors. *Stars and Stellar Systems*, Vol. VII, Chicago: Univ. Chicago Press; 1968, p. 221–364.
- [40] Isobe S. Evaporation of dirty ice particles surrounding early type stars. IV. Various size distributions. *Publ Astron Soc Japan* 1973;25:101–109.
- [41] Mathis JS, Rumpl W, Nordsieck KH. The size distribution of interstellar grains. *Astrophys J* 1977;217:425–433.
- [42] Wickramasinghe NC, Guillaume C. Interstellar extinction by graphite grains. *Nature* 1965;207:366–368.
- [43] Wickramasinghe NC, Nandy K. Optical properties of graphite–iron–silicate grain mixtures. *Mon Not R Astron Soc* 1971;153:205–227.
- [44] Wickramasinghe NC, Nandy K. Recent work on interstellar grains. *Rep Progr Phys* 1972;35:157–234.
- [45] Kim S-H, Martin PG, Hendry PD. The size distribution of interstellar dust particles as determined from extinction. *Astrophys J* 1994;422:164–175.
- [46] Mathis JS. Dust models with tight abundance constraints. *Astrophys J* 1996;472:643–655.
- [47] Zubko VG, Dwek E, Arendt G. Interstellar dust models consistent with extinction, emission, and abundance constraints. *Astrophys J Suppl Ser* 2004;152:211–249.

- [48] Zubko VG, Krełowski J, Wegner W. The size distribution of dust grains in single clouds — I. The analysis of extinction using multicomponent mixtures of bare spherical grains. *Mon Not R Astron Soc* 1996;283:577–588.
- [49] Zubko VG, Krełowski J, Wegner W. The size distribution of dust grains in single clouds — II. The analysis of extinction using inhomogeneous grains. *Mon Not R Astron Soc* 1998;294:548–556.
- [50] Wickramasinghe NC. On graphite particles as interstellar grains, II. *Mon Not R Astron Soc* 1963;126:99–114.
- [51] Wickramasinghe NC. Extinction curves for graphite–silicate grain mixtures. In: Houziaux L, Butler HE, editors. *Ultraviolet stellar spectra and ground based observations*, Dordrecht: Reidel; 1970; IAU Symp 36:42–49.
- [52] Greenberg JM, Li A. The core–mantle interstellar dust model. In: Greenberg JM, editor, *The Cosmic Dust Connection*, Dordrecht: Kluwer; 1996, p. 43–70.
- [53] Dorschner J, Henning Th. Dust metamorphosis in the galaxy. *Astron Astrophys Rev* 1995;6:271–333.
- [54] Farafonov VG, Il'in VB. Single light scattering: computational methods. In: Kokhanovsky AA, editor. *Light Scattering Reviews*, Berlin: Springer; 2006, vol. 1, p. 125–177.
- [55] Borghese F, Denti P, Saija R. *Scattering by model non-spherical particles*. 2nd ed. Heidelberg: Springer; 2007.
- [56] Min M. Optical properties of dust grains in the infrared: our view on cosmic dust. In: Henning Th, Grün E, Steinacker J, editors. *Cosmic Dust – Near and Far*, 2009, ASP Conf. Ser. vol. 414, p. 356–371.
- [57] Mathis JS, Whiffen G. Composite interstellar grains. *Astrophys J* 1989;341:808–822.
- [58] Vaidya DB, Gupta R, Dobbie JS, Chýlek P. Interstellar extinction by composite grains. *Astron Astrophys* 2001;375:584–590.

- [59] Gupta R, Mukai T, Vaidya DB, Sen AK, Okada Y. Interstellar extinction by spheroidal dust grains. *Astron Astrophys* 2005;441:555–561.
- [60] Voshchinnikov NV, Mathis JS. Calculating Cross Sections of Composite Interstellar Grains. *Astrophys J* 1999;526:257–264.
- [61] Voshchinnikov NV, Il'in VB, Henning Th, Dubkova DN. Dust extinction and absorption: the challenge of porous grains. *Astron Astrophys* 2006;445:167–177.
- [62] Iatì MA, Cecchi-Pestellini C, Williams DA, Borghese F, Denti P, Saija R. et al. Stratified dust grains in the interstellar medium – I. An accurate computational method for calculating their optical properties. *Mon Not R Astron Soc* 2008;384:591–598.
- [63] Farafonov VG, Voshchinnikov NV. Light scattering by a multilayered spheroidal particle. *Appl Opt* 2012;51:1586–1597.
- [64] Voshchinnikov NV, Il'in VB, Henning Th. Modelling the optical properties of composite and porous interstellar grains. *Astron Astrophys* 2005;429:371–381.
- [65] Li A. Can fluffy dust alleviate the subsolar interstellar abundance problem? *Astrophys J* 2005;622:965–969.
- [66] N.V. Voshchinnikov, and H.K. Das, Modelling interstellar extinction and polarization with spheroidal grains. *J Quantitative Spectrosc Rad Transfer* 2008;109:1527–1537.
- [67] Chini R, Krügel E. Abnormal extinction and dust properties in M 16, M 17, NGC 5357 and the Ophiuchus dark cloud. *Astron Astrophys* 1983;117:289–296.
- [68] Aannestad PA. Ultraviolet extinction to 10.8 inverse microns. *Astrophys J* 1995;443:653–663.
- [69] Li A, Greenberg JM. The dust extinction, polarization and emission in the high-latitude cloud toward HD 210121. *Astron Astrophys* 1998;339:591–600.

- [70] Larson KA, Wolff MJ, Roberge WG, Whittet DCB, He L. The size distribution of dust toward HD 210121 as determined from extinction. *Astrophys J* 2000;532:1021–1028.
- [71] Clayton GC, Wolff MJ, Sofia UJ, Gordon KD, Misselt KA. Dust grain size distributions from MRN to MEM. *Astrophys J* 2003;588:871–880.
- [72] Jones AP, Duley WW, Williams DA. The structure and evolution of hydrogenated amorphous carbon grains and mantles in the interstellar medium. *Quart J Roy Astron Soc* 1990;31:567–582.
- [73] Cecchi-Pestellini C, Iatì MA, Williams DA. The nature of interstellar dust as revealed by light scattering. this issue.
- [74] Hiltner WA. Polarization of light from distant stars by interstellar medium. *Science* 1949;109:165–165.
- [75] Hall JS. Observations of the polarized light from stars. *Science* 1949;109:166–167.
- [76] Dombrovskii VA. On the polarization of radiation of early-type stars. *Doklady Akad Nauk Armenia*. 1949;10:199–203.
- [77] Serkowski K. Interstellar polarization. In: Greenberg JM, Hayes DS, editors, *Interstellar Dust and Related Topics*, Dordrecht: Reidel; 1973, IAU Symp vol. 52, p. 145–152.
- [78] Serkowski K, Mathewson DS, Ford VL. Wavelength dependence of interstellar polarization and ratio of total to selective extinction. *Astrophys J* 1975;196:261–290.
- [79] Wolstencroft RD, Smith RJ. High precision spectropolarimetry of stars and planets — III. The wavelength dependence of interstellar polarization. *Mon Not R Astron Soc* 1984;208:461–480.
- [80] Efimov YuS. Interstellar polarization: new approximation. *Bull CrAO* 2009;105:82–114.
- [81] Whittet DCB, van Breda IG. The correlation of the interstellar extinction law with the wavelength of maximum polarization. *Astron Astrophys* 1978;66:57–63.

- [82] Whittet DCB, Gerakines PA, Hough JH, Shenoy SS. Interstellar extinction and polarization in the Taurus dark clouds: the optical properties of dust near the diffuse/dense cloud interface. *Astrophys J* 2001;547:872–884.
- [83] Andersson B-G, Potter SB. Observational constraints on interstellar grain alignment. *Astrophys J* 2007;665:369–389.
- [84] Whittet DCB, Martin PG, Hough JH, Rouse MF, Bailey JA, Axon DJ. Systematic variations in the wavelength dependence of interstellar linear polarization. *Astrophys J* 1992;386:562–577.
- [85] Martin PG, Adamson AJ, Whittet DCB, Hough JH, Bailey JA, Kim S-H. et al. Interstellar polarization from 3 to 5 microns in reddened stars. stars with extreme values of  $\lambda_{\max}$ . *Astrophys J* 1992;392:691–701.
- [86] Voshchinnikov NV, Yakovlev IS, Il'in VB, Das HK. Serkowski polarization curve calibrated with spheroidal grains. *Mon Not R Astron Soc* 2012; in preparation.
- [87] Rodrigues CV, Sartori MJ, Gregorio-Hetem J, Magalhães M. The alignment of the polarization Herbig Ae/Be stars with interstellar magnetic field. *Astrophys J* 2008;698:3031–2035.
- [88] Whittet DCB, Gerakines PA, Carkner AL, Hough JH, Martin PG, Prusti T. et al. A study of the Chamaeleon I dark cloud and T-association – VI. Interstellar polarization, grain alignment and magnetic field. *Mon Not R Astron Soc* 1994;268:1–12.
- [89] Voshchinnikov NV, Yakovlev IS. The relationship between grain shape and interstellar polarization. In: Muinonen K, Pehnttilä A, Lindquist H, Nousiainen T, Videen G, editors, *Electromagnetic and Light Scattering: Theory and Applications, XII*, Helsinki: University of Helsinki; 2010, p. 318–321.
- [90] Martin PG, Clayton GC, Wolff MJ. Ultraviolet interstellar linear polarization. V. Analysis of the final data set. *Astrophys J* 1999;510:905–914.
- [91] Wilking BA, Lebofsky MJ, Kemp JC, Martin PG, Rieke GH. The wavelength dependence of interstellar linear polarization. *Astrophys J* 1980;235:905–910.

- [92] Andersen CM, Weitenbeck AJ, Code AD, Nordsieck KH, Meade MR, Babler BL. et al. Ultraviolet interstellar linear polarization of galactic starlight I. Observations by the Wisconsin Ultraviolet Photo Polarimeter Experiment. *Astronom J* 1996;112:2726–2743.
- [93] Goodman AA, Jones TT, Lada EA, Myers PC. Does near-infrared polarimetry reveal the magnetic field in cold dark cloud? *Astrophys J* 1995;448:748–765.
- [94] Arce HG, Goodman AA, Bastien P, Manset N, Sumner M. The polarizing power of the interstellar medium in Taurus. *Astrophys J* 1998;499:L93–L97.
- [95] Gerakines PA, Whittet DCB, Lazarian A. Grain alignment in Taurus dark cloud. *Astrophys J* 1995;455:L71–L75.
- [96] Whittet DCB. Polarization observations of molecular clouds. In: Adamson A, Aspin C, Davis CJ, Fujiyoshi T, editors, *Astronomical Polarimetry: current status and future directions*. ASP Conf. Ser. 2005; v. 343: p. 321–331.
- [97] Whittet DCB, Hough JH, Lazarian A, Hoang T. The efficiency of grain alignment in dense interstellar clouds: a reassessment of constraints from near-infrared polarization. *Astrophys J* 2008;674:304–315.
- [98] Lazarian A, Goodman AA, Myers PC. On the efficiency of grain alignment in dark clouds. *Astrophys J* 1997;490:273–280.
- [99] Hough JH, Sato S, Tamura M, Yamashita T, McFadzean AD, Rouse MF. et al. Spectropolarimetry of the 3- $\mu\text{m}$  ice band in Elias 16 (Taurus Dark Cloud). *Mon Not R Astron Soc* 1988;230:107–115.
- [100] Hough JH, Aitken DK, Whittet DCB, Adamson AJ, Chrysostomou A. Grain alignment in dense cold environments: spectropolarimetry of the 4.67  $\mu\text{m}$  CO-ice feature in the field star Elias 16 (Taurus dark cloud). *Mon Not R Astron Soc* 2008;387:797–802.
- [101] Messenger DW, Whittet DCB, Roberge WG. Interstellar polarization in the Taurus dark clouds: wavelength-dependent position angles and cloud structure near TMC-1. *Astrophys J* 1997;487:314–319.

- [102] Bohren CF, Huffman DR. Absorption and Scattering of Light by Small Particles. John Wiley and Sons: New York: 1983.
- [103] Das HK, Voshchinnikov NV, Il'in VB. Interstellar extinction and polarization – A spheroidal dust grain approach perspective. *Mon Not R Astron Soc* 2010;404:265–274.
- [104] Wilson R. The relation between interstellar extinction and polarization. *Mon Not R Astron Soc* 1960;120:51–63.
- [105] Greenberg JM, Lind AC, Wang RT, Libelo LF. The polarization of starlight by oriented nonspherical particles. In: Kerker M, editor, *Electromagnetic Scattering*. New York: Pergamon Press; 1963; p. 123–134.
- [106] Greenberg JM, Shah G. A unified model of interstellar extinction and polarization. I. *Astrophys J* 1966;145:63–74.
- [107] Rogers C, Martin PG. On the shape of interstellar grains. *Astrophys J* 1979;228:450–464.
- [108] Hong SS, Greenberg JM. A unified model of interstellar grains: a connection between alignment efficiency, grain model size, and cosmic abundance. *Astron Astrophys* 1980;88:194–202.
- [109] Mathis JS. The size distribution of interstellar grains. II. Polarization. *Astrophys J* 1979;232:747–753.
- [110] Mathis JS. The alignment of interstellar grains. *Astrophys J* 1986;308:281–287.
- [111] Onaka T. Light scattering by spheroidal grains. *Ann Tokyo Astron Obs* 1980;18:1–54.
- [112] Vaidya DB, Bhatt HC, Desai JN. Interstellar extinction and polarization by spheroidal dust grains. *Astrophys Space Sci* 1984;104:323–336.
- [113] Voshchinnikov NV, Il'in AE, Il'in VB. Light extinction and polarization by dust grains in the interstellar medium: the interstellar linear polarization. *Astrophysics* 1986;24:299–305.

- [114] Voshchinnikov NV. Determination of and magnetic fields from polarimetric and photometric observations of stars. *Astron Nachr* 1989;310:265–271.
- [115] Mishchenko MI. Extinction and polarization of transmitted light by partially aligned nonspherical grains. *Astrophys J* 1991;367:561–574.
- [116] Wolff MJ, Clayton GC, Meade MR. Ultraviolet interstellar linear polarization I. Applicability of current grain models. *Astrophys J* 1993;403:722–735.
- [117] Kim S-H, Martin PG. The size distribution of interstellar dust particles as determined from polarization: infinite cylinders. *Astrophys J* 1994;431:783–796.
- [118] Kim S-H, Martin PG. The size distribution of interstellar dust particles as determined from polarization: spheroids. *Astrophys J* 1995;444:293–305.
- [119] Matsumura M, Seki M. Extinction and polarization by ellipsoidal particles in the infrared. *Astrophys J* 1996;456:557–565.
- [120] Li A, Greenberg JM, A unified model of interstellar dust. *Astron Astrophys* 1997;323:566–584.
- [121] Vaidya DB, Gupta R, Snow TP. Composite interstellar grains. *Mon Not R Astron Soc* 2007;379:791–800.
- [122] Wurm G, Schnaiter M. Coagulation as unifying element for interstellar polarization. *Astrophys J* 2002;567:370–375.
- [123] Voshchinnikov NV. Optical properties of the spheroidal dust grains. Forward transmitted radiation. *Sov Astron* 1990;34:535–541.
- [124] Voshchinnikov NV, Farafonov VG. Optical properties of spheroidal particles. *Astrophys Space Sci* 1993;204:19–86.
- [125] Draine BT, Fraisse AA. Polarized far-infrared and submillimeter emission from interstellar grains. *Astrophys J* 2009;626:1–11.
- [126] Wickramasinghe NC. Light scattering functions with applications in astronomy. Hilger: 1973.

- [127] Asano S. Light scattering properties of spheroidal particles. *Appl Optics* 1979;18:712-723.
- [128] Lind AC, Greenberg JM. Electromagnetic scattering by obliquely oriented cylinders. *J Appl Phys* 1966;37:3195–3203.
- [129] Shah GA. Scattering of plane electromagnetic waves by infinite concentric circular cylinders at oblique incidence. *Mon Not R Astron Soc* 1970;148:93–102.
- [130] Asano S, Yamamoto G. Light scattering a spheroidal particle. *Appl Optics* 1975;14:29-49.
- [131] Draine BT. The Discrete Dipole Approximation for light scattering by irregular targets. In: Mishchenko MI, Hovenier JW, Travis LD, editors. *Light Scattering by Nonspherical Particles*, San Francisco: Academic Press; 2000, p. 131–145.
- [132] Hovenier JW, Lumme K, Mishchenko MI, Voshchinnikov NV, Mackowski DW, Rahola J. Computations of scattering matrices of four types of non-spherical particles using diverse methods. *J Quant Spectrosc Radiat Transfer* 1996;55:695–705.
- [133] Voshchinnikov NV, Il'in VB, Henning Th, Michel B, Farafonov VG. Extinction and Polarization of Radiation by Absorbing Spheroids: Shape/Size Effects and Some Benchmarks. *J Quant Spectrosc Radiat Transfer* 2000;65:877–893.
- [134] Krügel, E. *The Physics of Interstellar Dust* London: Institute of Physics Publishing; 2003.
- [135] Davis L, Greenstein JL. The polarization of starlight by aligned dust grains. *Astrophys J* 1951;114:206–239.
- [136] Roberge WG, Lazarian A. Davis–Greenstein alignment of oblate spheroidal grains. *Mon Not R Astron Soc* 1999;305:615–630.
- [137] Heiles C, Crutcher R. Magnetic Fields in Diffuse H I and Molecular Clouds. In: Wielebinski R, Beck R, editors. *Cosmic Magnetic Fields*, Berlin: Springer; 2005, *Lect Notes Phys* 664, p. 137–182.

- [138] Jones RV, Spitzer L. Magnetic alignment of interstellar grains. *Astrophys J* 1967;147:943–964.
- [139] Djouadi G, Gattacecca J, d’Hendecourt L, Rochette P, Jones AP, Davoisne C. et al. Ferromagnetic inclusions in silicate thin films: insights into the magnetic properties of cosmic grains. *Astron Astrophys* 2007;468:L9–L13.
- [140] Belley F, Ferré EC, Martín-Hernández F, Jackson MJ, Dyar MD, Catlos EJ. The magnetic properties of natural and synthetic  $(\text{Fe}_x, \text{Mg}_{1-x})_2\text{SiO}_4$  olivines. *Earth Plan Sci Lett* 2009;284:516–526.
- [141] Duley WW. Magnetic alignment of interstellar grains. *Astrophys J* 1978;219:L129–L132.
- [142] Sorrell WH. Origin of superparamagnetism in core–mantle grains. *Mon Not R Astron Soc* 1994;268:40–48.
- [143] Sorrell WH. Interstellar polarization and magnetic alignment of pin-wheel dust grains. II. Grain alignment efficiency. *Mon Not R Astron Soc* 1995;273:187–200.
- [144] Lazarian A, Hoang T. Alignment of dust with magnetic inclusions: radiative torques and superparamagnetic Barnett and nuclear relaxation. *Astrophys J* 2008;676:L25–L28.
- [145] Lazarian A, Hoang T. Radiative torques: analytical model and basic properties. *Mon Not R Astron Soc* 2007;378:910–946.
- [146] Andersson B-G, Potter SB. Observations of enhanced radiative grain alignment near HD 97300. *Astrophys J* 2010;720:1045–1054.
- [147] Matsumura M, Kameura Y, Kawabata KS, Akitaya H, Isogai M, Seki M. Correlation between interstellar polarization and dust temperature: alignment of grains by radiative torques is ubiquitous? *Publ Astron Soc Japan* 2011;63:L43–L47.
- [148] Andersson B-G, Pintado O, Potter SB, Straižys V, Charcos-Llorens M. Angle–dependent radiative grain alignment. Confirmation of a magnetic field — radiation anisotropy angle dependence on the efficiency of interstellar grain alignment. *Astron Astrophys* 2011;534:A19(6pp).

- [149] Dolginov AZ, Gnedin YuN, Silant'ev NA. Propagation and Polarization of Radiation in Cosmic Medium. Moscow: Nauka; 1979.
- [150] Voshchinnikov NV, Henning Th, Prokopjeva MS, Das HK. Interstellar polarization and grain alignment: the role of iron and silicon. *Astron Astrophys* 2012;541:A52(10pp).
- [151] Hough JH, Aitken DK. Infrared polarimetry of interstellar dust. In: Videen G, Yatskiv Y, Mishchenko M, editors. *Photopolarimetry in Remote Sensing*, NATO Science Series 2004; v. 161: p. 325–350.
- [152] Chair JE, Adamson AJ, Whittet DCB, Chrysostomou A, Hough JH, Kerr TH. et al. Sectropolarimetry of the 3.4  $\mu\text{m}$  feature in the diffuse ISM toward the Galactic center quintuplet cluster. *Astrophys J* 2006;651:268–271.
- [153] Kenyon SJ, Gómez M, Whitney BA. Low mass star formation in the Taurus–Auriga clouds. In: Reipurth B, editor. *Handbook of star forming regions*. ASP 2008; v. 1: p. 405–458.
- [154] Dobashi K, Uehara H, Kandori R, Sakurai T, Kaiden M. Atlas and catalog of dark clouds based on digitized sky survey I. *Publ Astron Soc Japan* 2005;57:S1–S386.
- [155] Straizys V, Meistas E. Interstellar extinction in the dark Taurus clouds. I. *Acta Astron* 1980;30:541–552.
- [156] Padoan P, Cambrésy L, Langer W. Structure function scaling of a 2MASS extinction map of Taurus. *Astrophys J* 2002;580:L57–L60.
- [157] Schloerb FP, Snell RL. Large-scale structure of molecular gas in Heiles Cloud 2: a remarkable rotating ring. *Astrophys J* 1984;283:129–139.
- [158] Gaida M, Ungerechts H, Winnewisser G. Ammonia observations and star counts in the Taurus dark cloud complex. *Astron Astrophys* 1984;137:17–25.
- [159] Crutcher RM. Optical and radio study of the Taurus molecular cloud toward HD 29647. *Astrophys J* 1985;288:604–617.

- [160] Heyer MH, Vrba FJ, Snell RL, Schloerb FP, Strom SE, Goldsmith PF. et al. The magnetic evolution of the Taurus molecular clouds. I. Large-scale properties. *Astrophys J* 1987;321:855–876.
- [161] Goldsmith PF, Heyer MH, Narayanan G, Snell R, Li D, Brunt C. Large-scale structure of the molecular gas in Taurus revealed by high linear dynamic range spectral line mapping. *Astrophys J* 2008;680:428–445.
- [162] Moneti A, Pipher JL, Helfer HL, McMillan RS, Perry ML. Magnetic field structure in the Taurus dark cloud. *Astrophys J* 1984;282:508–515.
- [163] Goodman AA, Bastien P, Myers PC, Ménard F. Optical polarization maps of star-forming regions in Perseus, Taurus, and Ophiuchus. *Astrophys J* 1990;359:363–377.
- [164] Tamura M, Nagata T, Sato S, Tanaka M. Infrared polarimetry of dark clouds – I. Magnetic field structure in Heiles Cloud 2. *Mon Not R Astron Soc* 1987;224:413–423.
- [165] Goodman AA, Jones TJ, Lada EA, Myers PC. The structure of magnetic fields in dark cloud: infrared polarimetry in B216–217. *Astrophys J* 1992;399:108–113.
- [166] Chapman NL, Goldsmith PF, Pineda JL, Clemens DP, Li D, Krčo M. The magnetic field in Taurus probed by infrared polarization. *Astrophys J* 2011;741:21(20pp).
- [167] Whittet DCB, Shenoy SS, Clayton Gc, Gordon KD. The ultraviolet extinction curve of intraclump dust in Taurus (TMC-1): constraints on the 2175 Å bump absorber. *Astrophys J* 2004;602:291–297.
- [168] Aannestad PA, Greenberg JM. Interstellar polarization, grain growth, and alignment. *Astrophys J* 1983;272:551–562.
- [169] Lee D-H, Yuk I-S, Jin H, Seon K-I, Edelstein J, Korpela J. et al. Diffuse far-ultraviolet observations of the Taurus region. *Astrophys J* 2006;644:L181–L184.
- [170] Turner BE, Heiles C. The C<sub>4</sub>H Zeeman effect in TMC-1: understanding low-mass star formation. *Astrophys J Suppl Ser* 2006;162:388–400.

- [171] Crutcher RM, Wandelt B, Heiles C, Falgarone E, Troland TH. Magnetic fields in interstellar clouds from Zeeman observations: interference of total field strengths by Bayesian analysis. *Astrophys J* 2010;725:466–479.

